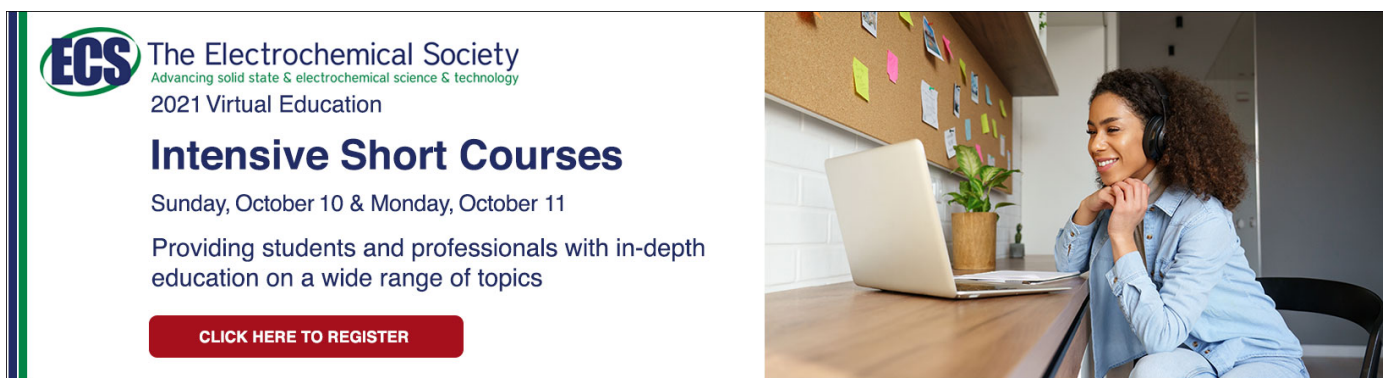


PAPER

CMOS-MEMS technologies for the applications of environment sensors and environment sensing hubs

To cite this article: Ya-Chu Lee *et al* 2021 *J. Micromech. Microeng.* **31** 074004

View the [article online](#) for updates and enhancements.



ECS The Electrochemical Society
Advancing solid state & electrochemical science & technology
2021 Virtual Education

Intensive Short Courses

Sunday, October 10 & Monday, October 11

Providing students and professionals with in-depth education on a wide range of topics

[CLICK HERE TO REGISTER](#)



CMOS-MEMS technologies for the applications of environment sensors and environment sensing hubs

Ya-Chu Lee¹, Meng-Lin Hsieh¹, Pen-Sheng Lin¹, Chia-Hung Yang¹, Sheng-Kai Yeh¹, Thi Thu Do² and Weileun Fang^{1,2,*} 

¹ Power Mechanical Engineering, National Tsing Hua University, Hsinchu, Taiwan

² Institute of NanoEngineering and MicroSystems, National Tsing Hua University, Hsinchu, Taiwan

E-mail: fang@pme.nthu.edu.tw

Received 4 March 2021, revised 12 April 2021

Accepted for publication 25 May 2021

Published 10 June 2021



CrossMark

Abstract

The booming growth in environmental conditions sensing and monitoring pushes the need of inexpensive environment sensors with small size and low power consumption. The outbreak of COVID-19 further increases the need for fast monitoring of environment conditions. The micro-electrical-mechanical-systems (MEMS) technologies are considered as promising solutions to realize the required environment sensors. The mature complementary metal-oxide-semiconductor (CMOS) process platforms available in many foundries can be extended to fabricate MEMS sensors to offer the advantage of relatively easier commercialization. Moreover, by leveraging the characteristics of CMOS process platforms, the integration of multiple sensors and sensing circuits to form a compact sensing system can also be achieved. This review paper will focus on introducing the miniaturized environmental sensing devices implemented and integrated using the CMOS-MEMS technologies. In general, the CMOS chips for environment sensing are firstly fabricated using the foundry-available CMOS processes, and then the post-CMOS micromachining processes are performed to implement the CMOS-MEMS environment sensors. This paper respectively reviews five different environment sensors (including the infrared, pressure (barometer), humidity/temperature, and gas sensors) using the CMOS-based MEMS technologies. The advantages and design concerns of sensors fabricated by different CMOS and post-CMOS processes are introduced and discussed. Moreover, the CMOS-MEMS environment sensing hub implemented through the monolithic integration of multiple environment sensors is also introduced.

Keywords: CMOS, CMOS MEMS, environment sensor, IR sensor, barometer, humidity sensor, gas sensor

(Some figures may appear in colour only in the online journal)

1. Introduction

The environment conditions and trends are important information to not only the daily life, but also in various applications, such as the agriculture, industry, health care, and so on. In these applications, environmental monitoring systems

can help to provide vital information, for example humidity, pressure, temperature, gas, and particle, about the surroundings. Especially due to the tremendous disruption brought upon by the outbreak of the novel coronavirus (COVID-19), the increasing need for medical environmental monitoring to enhance safety of the society during this pandemic is paramount. Thus, environmental monitoring is becoming a critical need for the prosperity of present and future generations. To date, many different sensors have been developed to address

* Author to whom any correspondence should be addressed.

the increasing need for environmental monitoring, yet, when implemented for real-world use, these products are often faced with challenges regarding their costs, sizes, and power consumptions. These challenges will limit the adoption of these sensors for a variety of applications, and inhibit the potential fulfillment of the rapidly growing environmental monitoring market. For example, due to its size, traditional humidity sensing psychrometers used in meteorological stations are unsuitable for use in applications such as handheld consumer electronics; for the same reason, traditional industrial waste detection systems are also hard to implement in wider environmental monitoring applications. Therefore, to leverage the mature semiconductor technologies to implement the environment sensing devices is considered as a potential solution to properly resolve the aforementioned challenges, such as the issues of size, cost, power consumption, and so on.

The semiconductor fabrication technologies have been successfully extended to realize chip-scale micro-electrical-mechanical-systems (MEMS), including miniaturized sensors [1, 2] and actuators [3, 4]. As brought by the considerable advancements in the MEMS industry, numerous devices for different applications have been developed and commercialized to benefit everyday life, for example, the various MEMS pressure sensors [5], accelerometers [6], or gyroscopes [7] that are employed in automotive industry to enhance driving safety and comfort. The MEMS microphones [8, 9], accelerometers [7, 10], humidity sensors [11], pressure sensors [5], have also been extensively employed in smart phones to offer more functions as well as to enhance human-machine interactions. Moreover, the smart wearable devices equipped with the optical sensor for heart rate monitoring [12, 13] are also available now. To date, MEMS continues to provide contributions in many applications due to its features of being miniaturized, low cost, low power consumption, and so on. Thus, MEMS technology is also considered as a promising approach for the further development of environmental monitoring. Various MEMS environment sensors have already been developed, such as humidity [14, 15], pressure [5, 16–18], temperature [19], infrared (IR) [20–23], gas [24, 25], etc, sensors, and have also been commercialized into available products in [26]. In short, MEMS will be a key enabling technology in the future progress of environmental sensing.

Presently, various Si-based MEMS fabrication technologies have been reported, for instance, the surface/bulk micromachining [27, 28], silicon-on-insulator (SOI) and cavity SOI processes [29], complementary metal-oxide-semiconductor (CMOS) MEMS [30], etc. Among these fabrication technologies, CMOS-MEMS approach exploits the standard commercial semiconductor process platforms to implement micro sensors and actuators, and hence the mature semiconductor technologies and supply chain can be leveraged to effectively reduce the time and efforts for commercialization. Numerous CMOS-MEMS devices have been demonstrated using different commercial platforms, for example, the tactile sensor [31], magnetic sensor [32] and accelerometer [33] from the *TSMC* (Taiwan Semiconductor Manufacturing Co., Taiwan) 2P4M (in this review: ‘P’ and ‘M’ respectively stand for ‘Poly-Si’ and ‘Metal’, ‘2P4M’ means the process

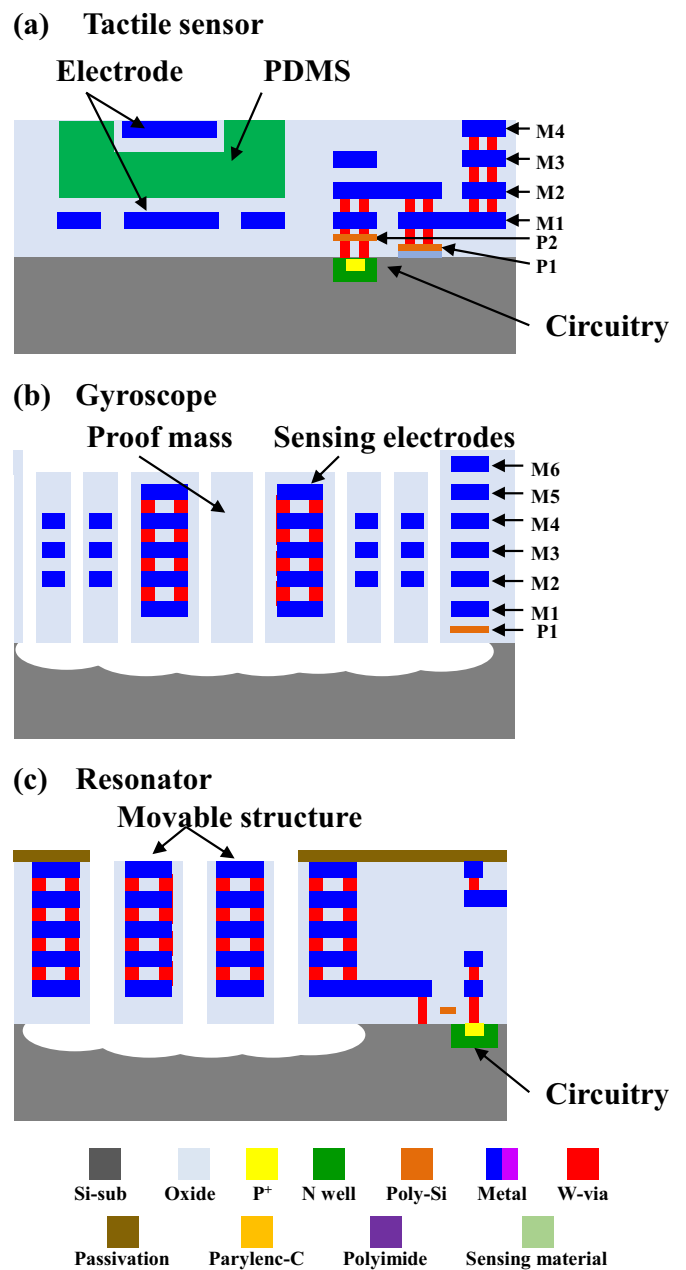


Figure 1. Typical commercial standard CMOS processes: (a) TSMC 0.35 μm 2P4M CMOS process, (b) TSMC 0.18 μm 1P6M CMOS process, and (c) UMC 0.18 μm 1P6M CMOS process.

consisted of two poly-Si and four metal layers) standard process shown in figure 1(a), the gyroscope [34], microphones [35] and tactile sensors [36] from the *TSMC* 1P6M process displayed in figure 1(b), and the RF devices [37, 38] and fingerprint sensors [39] from the *UMC* (United Microelectronics Co., Taiwan) 0.18 μm 1P6M CMOS process depicted in figure 1(c). By using the existing CMOS platforms, many environmental sensing chips have also been developed, which include sensors for the detection of temperature, pressure, IR, gas, PM 2.5 [40], etc. Moreover, the commercially available CMOS-MEMS environment sensing chips, such as the humidity sensor [11], barometer [41], and IR sensor [20–23], have been demonstrated by companies. In general, the thin

film materials inherent in the CMOS processes could enable various sensing mechanisms such as capacitive, piezoresistive, thermoelectric, etc, moreover, the multiple metal/dielectric layers for the CMOS back-end-of-line (BEOL) processes could be exploited to fabricate MEMS structures. Apart from being able to fabricate different kinds of environmental monitoring devices, the CMOS platform also possesses the distinctive potential for system-on-chip (SoC) integration. Using the CMOS platform, different MEMS devices can be monolithically integrated onto the same chip to form ‘sensing hubs’ or ‘partial sensors’, and can even be integrated with dedicated circuitry to form complete sensing systems. These benefits enable the CMOS-MEMS to be especially suited for future applications in environmental monitoring, in which the widely available environmental monitoring devices can be selectively integrated and fabricated depending on different applications.

Therefore, this review paper will focus on introducing the miniaturized environmental sensing devices implemented and integrated using the CMOS-MEMS technologies. In general, the CMOS chips for environment sensing are firstly fabricated using the foundry-available CMOS processes offered by the *TSMC*, *UMC*, *X-FAB* (X-FAB Semiconductor Foundries AG, Germany), *ams* (ams AG, Austria), *Semefab* (Semefab, UK), *SMIC* (Semiconductor Manufacturing International Co., China), and so on. The design of these CMOS chips has to follow the design-rules provided by foundries. After that, the post-CMOS micromachining processes are performed to implement the CMOS-MEMS environment sensors. In this review paper, the thermoelectric and bolometer types of CMOS-MEMS IR sensors will be discussed in section 2. After that, section 3 will review various approaches to realize the capacitive and piezoresistive CMOS-MEMS pressure sensors. In addition, the design of humidity CMOS-MEMS sensors and their integration with temperature sensors will be introduced in section 4. Section 5 will show the CMOS-MEMS gas sensors, mainly chemo-resistive type together with some other sensing mechanisms. Each section will introduce the CMOS-based MEMS processes and their development for these environmental sensors, and also provide the key benefits as well as challenges of using CMOS platform for developing these environmental sensors. Besides, the design concerns regarding the fabrication processes and application of sensors are also commented and summarized. Moreover, section 6 will further discuss the monolithic integration of multiple environment sensors to achieve the environment sensing hub by using the CMOS-MEMS technology. Finally, conclusions and future outlook on the overall scope of CMOS-MEMS environmental sensors are concluded in section 7.

2. Infrared (IR) sensors

The IR sensors are used to transfer IR intensity into electrical signal and have been widely applied in many applications including thermometer, thermal imaging and night vision cameras, motion detection, and gas sensing. MEMS IR sensors, also known as uncooled IR sensors, are fabricated through micromachining technologies to achieve compact device sizes,

low-power consumption, and low cost. As shown in figure 2, the typical MEMS IR sensor consists of three components suspended on the silicon substrate: the IR absorber, the thermal-isolation structure, and the temperature sensing material/unit (such as thermoelectric materials in figure 2(a) or diodes in figure 2(b)). In addition, the temperature coefficient of resistance (TCR) for thin films has also been applied for temperature sensing. In this review, these sensing films are named ‘TCR materials’ for short. In general, the incident radiation is absorbed by IR absorbers to cause a temperature change and further lead the variation of electrical signals through different sensing materials/units [42–44]. Thus, the IR intensity can be determined by the electrical signal detected by the sensor. The CMOS platforms possess various functional materials to realize different MEMS IR sensors [45–47]. The BEOL layers of the CMOS platforms also enable the design of novel structures for IR absorption and thermal isolation. Moreover, as being a mature IC platform, CMOS processes are able to integrate application specific integrated circuits (ASICs) with MEMS IR sensors, and further push the trend of CMOS-MEMS IR sensors.

The gain flow charts in figure 2 indicate that a higher rising temperature ΔT of the sensor contributed from the incident IR could offer a larger sensing signal for both detection mechanisms, thermoelectric and bolometric. The temperature elevation ΔT of the sensor is influenced by: (1) the IR absorptivity (α_{absorb}) and (2) the thermal resistances (R_{th}) of the sensor determined from the thermal loss through the thermal radiation, air conduction, and solid conduction [48]. The suspended structures achieved by MEMS technologies could prevent the significant thermal loss from the silicon substrate. Moreover, the design of absorber structure/material could increase the IR absorptivity, while the design of thermal-isolation structure could enhance the thermal resistance of the sensor. Thus, the designs of thermal-isolation and IR absorbing structures/materials are critical to the temperature elevation of the sensor. The thermal loss through the air conduction can be further suppressed by the vacuum packaging. In this review, the sensing mechanisms, thermal-isolation structures, and IR absorbing structures/materials of CMOS-MEMS IR sensors will be discussed in the following sub-sections. Moreover, according to the compatible and available materials for CMOS platforms, the sensing mechanisms of CMOS-MEMS IR sensors can be characterized into thermoelectric type [44–47, 49–58] and bolometer type [43, 59–66]. Thus, the CMOS-MEMS IR sensors based on these two different sensing mechanisms will be discussed respectively.

2.1. Thermoelectric type CMOS-MEMS IR sensors

Figure 2(a) displays a typical architecture of thermoelectric type MEMS IR sensor which consists of the IR absorber, and the thermal-isolation structure with embedded thermoelectric material. The absorber is supported by the thermal-isolation structure which is anchored to the substrate. These components are suspended on the substrate to avoid the thermal loss by heat conduction through silicon wafer. As IR is incident on the sensor, the temperature of the absorber will rise and lead

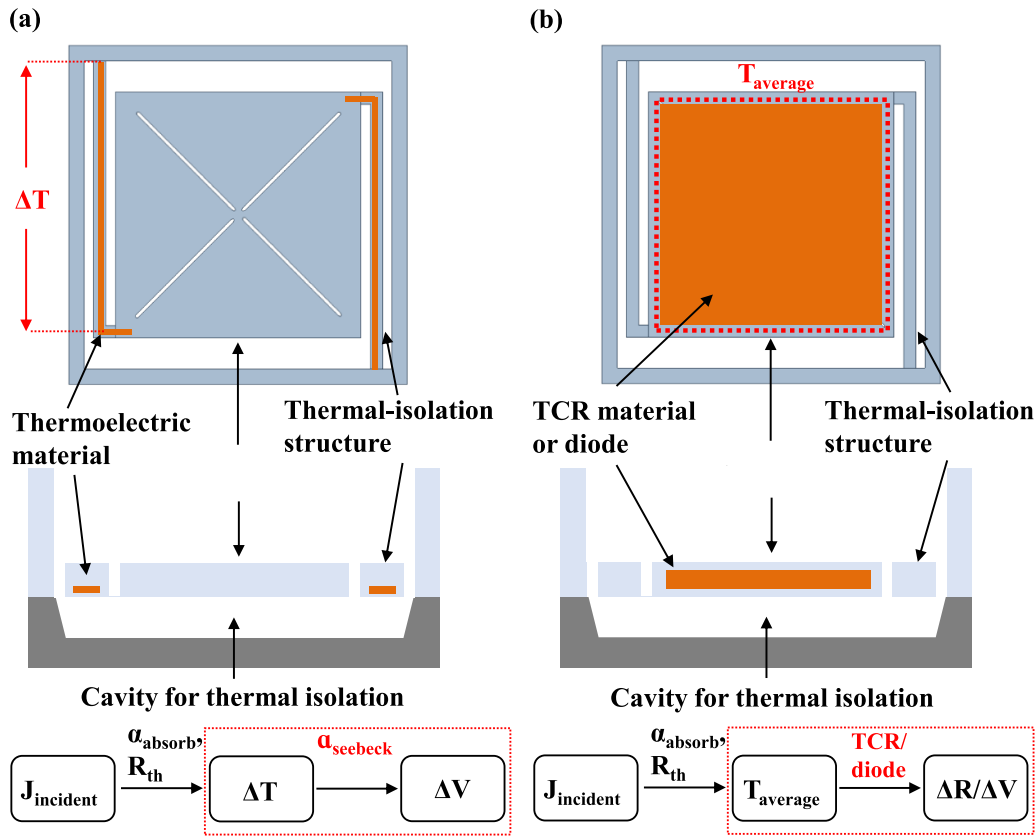


Figure 2. The schematic illustrations and gain flow charts of MEMS IR sensor: (a) thermoelectric type and (b) bolometer type.

to a ΔT between the two ends of its support (thermal-isolation structure). Thus, the thermoelectric material embedded in the thermal-isolation structure could detect the temperature difference and be used to determine the absorbed IR. Such temperature detection technology of thermoelectric materials is known as the Seebeck effect [67], and the ratio of voltage difference to temperature difference is called the Seebeck coefficient. Note that semiconductor materials such as the poly-Si layer available in the CMOS platforms have a superior Seebeck coefficient.

Various thermoelectric materials are available in the CMOS platforms such as the AlCu, P-doped poly-Si, and N-doped poly-Si. The AlCu and the P-doped poly-Si show positive Seebeck coefficient, whereas the N-doped poly-Si shows negative Seebeck coefficient. In this regard, CMOS-MEMS thermoelectric IR sensors (named thermocouples) based on different combination of available thermoelectric materials are proposed to increase the net Seebeck coefficient, including the AlCu/N-type poly-Si in figure 3(a) [46, 49, 54, 58], and the P-type/N-type poly-Si in figure 3(b) [44, 45, 47, 50, 51, 53, 56, 57]. In addition to the conventional CMOS processes, the thermoelectric IR sensor with P-type/N-type single crystal Si thermocouples in figure 3(c) has been realized by using the device layer of SOI-CMOS process [68]. The Au/N-type poly-Si thermopile has also been developed by using the in-house CMOS processes [52], yet Au is a prohibited material in commercial CMOS foundry. It is worth to note that silicide layers are commonly employed in the commercial CMOS platforms

to deposit on poly-Si layers for reducing the contact resistance between poly-Si and metal layers. However, these layers decrease the Seebeck coefficient of poly-Si thermocouples causing lower responsivity of CMOS-MEMS thermoelectric IR sensors. The approach to increase the Seebeck coefficient as well as responsivities of CMOS-MEMS IR sensors by removing silicide layers is demonstrated in [44]. Moreover, the number of thermocouples will increase the output signal of thermoelectric IR sensors. To increase the number of thermocouples is a design concern for the thermoelectric IR sensors.

2.1.1. Structure designs for R_{th} and thermocouple arrangement. To date, various suspended mechanical structures have been demonstrated by using the BEOL layers of CMOS processes for different applications. This sub-section will firstly review existing structure designs including the fully clamped membranes [69, 70], the cantilever beams [49, 71], and serpentine structures [50, 51, 59] for the application of thermoelectric type CMOS-MEMS IR sensors. The design concerns are mainly (1) the thermal resistance R_{th} of the structure and (2) the number of thermocouples N to arrange in the structure. As shown in figure 4(a), the fully clamped circular diaphragm with its whole boundaries anchored to the Si substrate (i.e. the heat sink) is employed in the designs of [69, 70]. Such a structure has also been extensively applied in MEMS transducers [72]. Although thermal-isolation structures cannot be clearly indicated in this design, the center and boundary

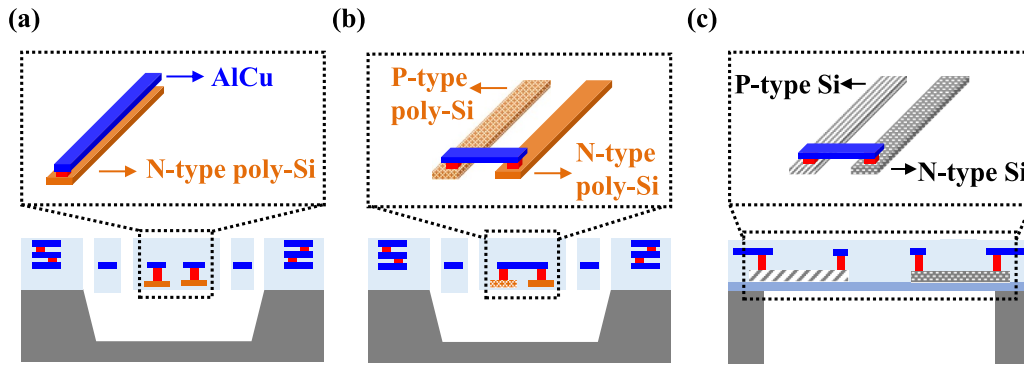


Figure 3. The schematic illustrations of the CMOS-MEMS thermoelectric IR sensors based on different combination of thermoelectric materials: (a) AICu/N-type poly-Si, (b) P-type/N-type poly-Si, and (c) P-type/N-type single crystal Si.

(connected to the heat sink) of the diaphragm still exhibit temperature difference (ΔT) after absorbing IR as depicted in figure 4(a). Thus, the thermocouple can be arranged in radial direction to provide the thermoelectric signal. Such design has larger structure area to allocate thermocouples and broader boundaries for flexible electric routings. However, the heat loss through the broader boundary may cause a poor thermal resistance. In terms of the fabrication processes, the back-side Si etching [70] or the etching release holes [69] are required to fabricate the fully-clamped diaphragm. Next, as shown in figure 4(b), the well-known MEMS cantilever [73] is another suspended structure for CMOS-MEMS IR sensor [71]. For cantilever, thermal-isolation structures also cannot be clearly distinguished. However, as shown in figure 4(b), the free-end and fixed-end (connect to the heat sink) of the cantilever has temperature difference (ΔT) after absorbing IR. Thus, the thermocouples can be arranged along the beam-length direction to provide the thermoelectric signal. Note that, for a given footprint A of the cantilever ($A = L \times W$), a longer beam length L could enhance the thermal resistance R_{th} to increase the ΔT , whereas a wider beam width W could increase the number N of thermocouples. In comparison, the cantilever, with only one edge anchored to the substrate, has higher thermal resistance than the fully-clamped diaphragm. Moreover, the cantilever structure can be easily released through the front-side bulk Si etching. As shown in figure 4(c), the serpentine structures are proposed in [55] to further facilitate the thermal resistance of MEMS IR sensors under the same footprint. The serpentine design could increase the equivalent length between the beam center and the fixed-end, so that the path for heat transfer is also increased to reduce the thermal loss of the structure. In short, the serpentine beam acts as the thermal-isolation structure to enhance the temperature difference (ΔT) between the two ends of the thermocouple. The shape and dimensions of the serpentine structure are critical design concerns that influence the thermal resistance R_{th} and the number N of thermocouples. In this regard, various serpentine structures have been designed to enhance the sensing signal of thermoelectric CMOS-MEMS IR sensor [50, 51, 59]. As shown in figure 5(a), the novel serpentine structure was developed to increase the thermal resistance between the center (T_{high}) to the boundary (T_{low}), so as to increase the ΔT [50]. The serpentine structure

with embedded thermocouples is fabricated using the *TSMC* 0.35 μm 2P4M process and then released from the Si substrate by the XeF_2 isotropic etching through strip-shaped holes. The disadvantage of this design is the reduced number N of thermocouples. Figure 5(b) displays another serpentine structure, and again the design is to find a better arrangement for the thermal resistance R_{th} and the number N of thermocouples [51]. On the other hand, the electrical resistance as well as the resistor noise will be increased when the length of thermocouple is increased with the serpentine beam length. Therefore, to improve the signal to noise ratio of the thermoelectric CMOS-MEMS IR sensor, the serpentine structures need to be optimized to balance the trade-off between the thermal resistance and the electrical resistance [59].

2.1.2. Material and structure designs for IR absorbing. In addition to the thermal resistances R_{th} of the suspended structures, the IR absorptivity α_{absorb} of the absorber is another critical concern to enhance the performance of CMOS-MEMS IR sensors. Typically, the dielectric layers inherent in the CMOS BEOL (such as SiO_2 and Si_3N_4 films) are exploited as the absorber for the CMOS-MEMS IR sensors [44, 52, 74]. To further enhance the IR absorption, the approaches of adding additional structures or depositing new materials have been investigated. As shown in figure 6(a), an additional umbrella-like structure is fabricated and vertically integrated with the serpentine thermal-isolation structure by using the *TSMC* 0.18 μm 1P6M [44] to enhance the performance of the IR sensor. The umbrella-like structure and the absorber are formed by the CMOS BEOL layers. The IR absorption area of the umbrella-like structure can be increased since no strip-shaped holes (to increase the thermal resistance, as shown in figure 5(a)) are required. Moreover, after the incident of IR, the temperature elevation of the absorber is the result of the heat transfer from the umbrella-like structure through the post. Thus, the T_{high} of thermocouples can be increased by the design of the umbrella-like structure. However, the absorptivity of dielectric layers as well as their targeted absorption wavelengths are still limited by the material properties. Therefore, as displayed in figure 6(b), porous materials such as Au-black were dropped or deposited on CMOS-MEMS IR

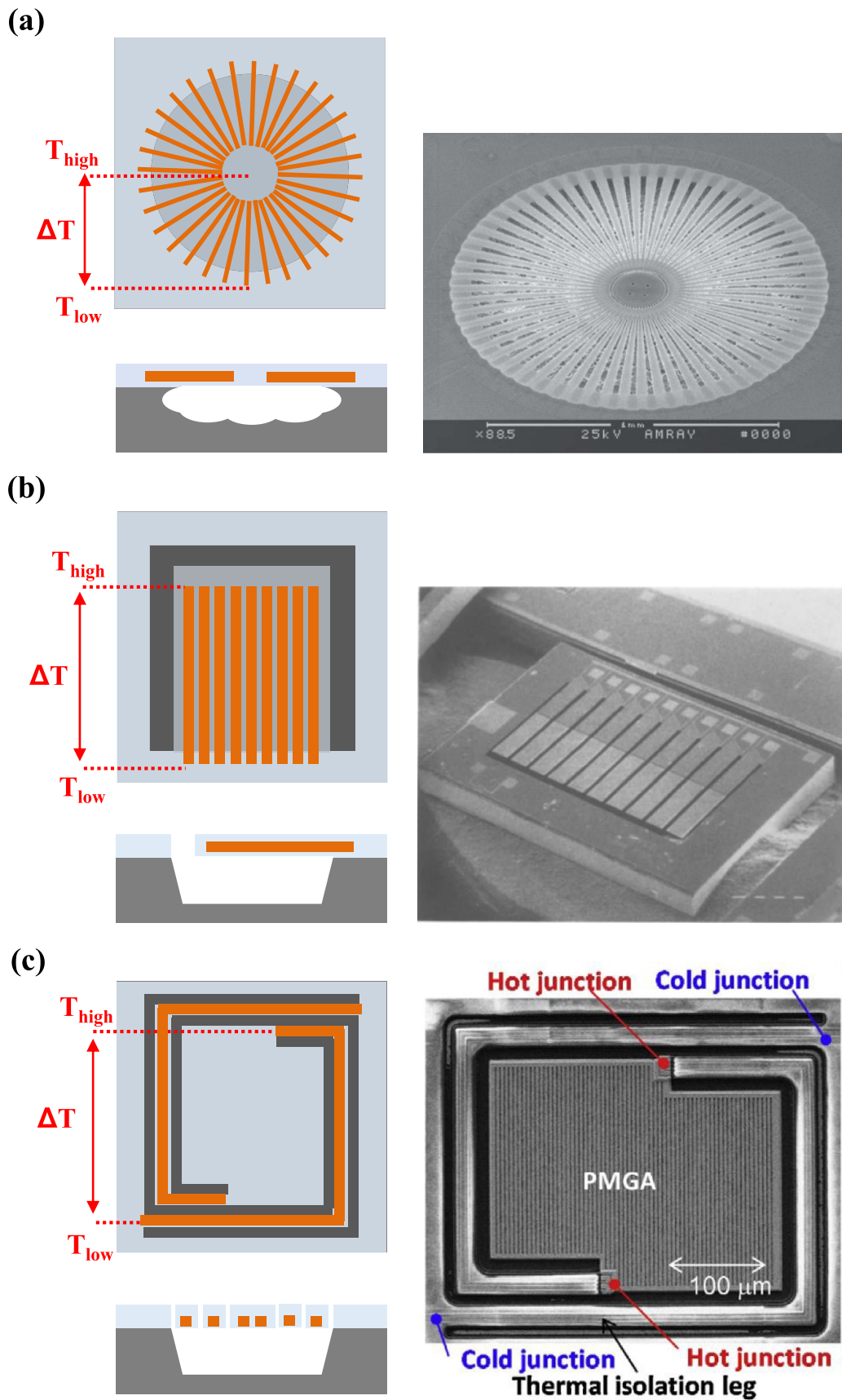


Figure 4. The schematic illustrations and SEM micrographs of three structure designs for R_{th} and thermocouple arrangement: (a) fully clamped membranes [69]. Reproduced from [69]. © IOP Publishing Ltd. All rights reserved. (b) Cantilever beams [71]. Reprinted from [71], Copyright (1989), with permission from Elsevier. (c) Serpentine structures [55]. Reprinted from [55], Copyright (2018), with permission from Elsevier.

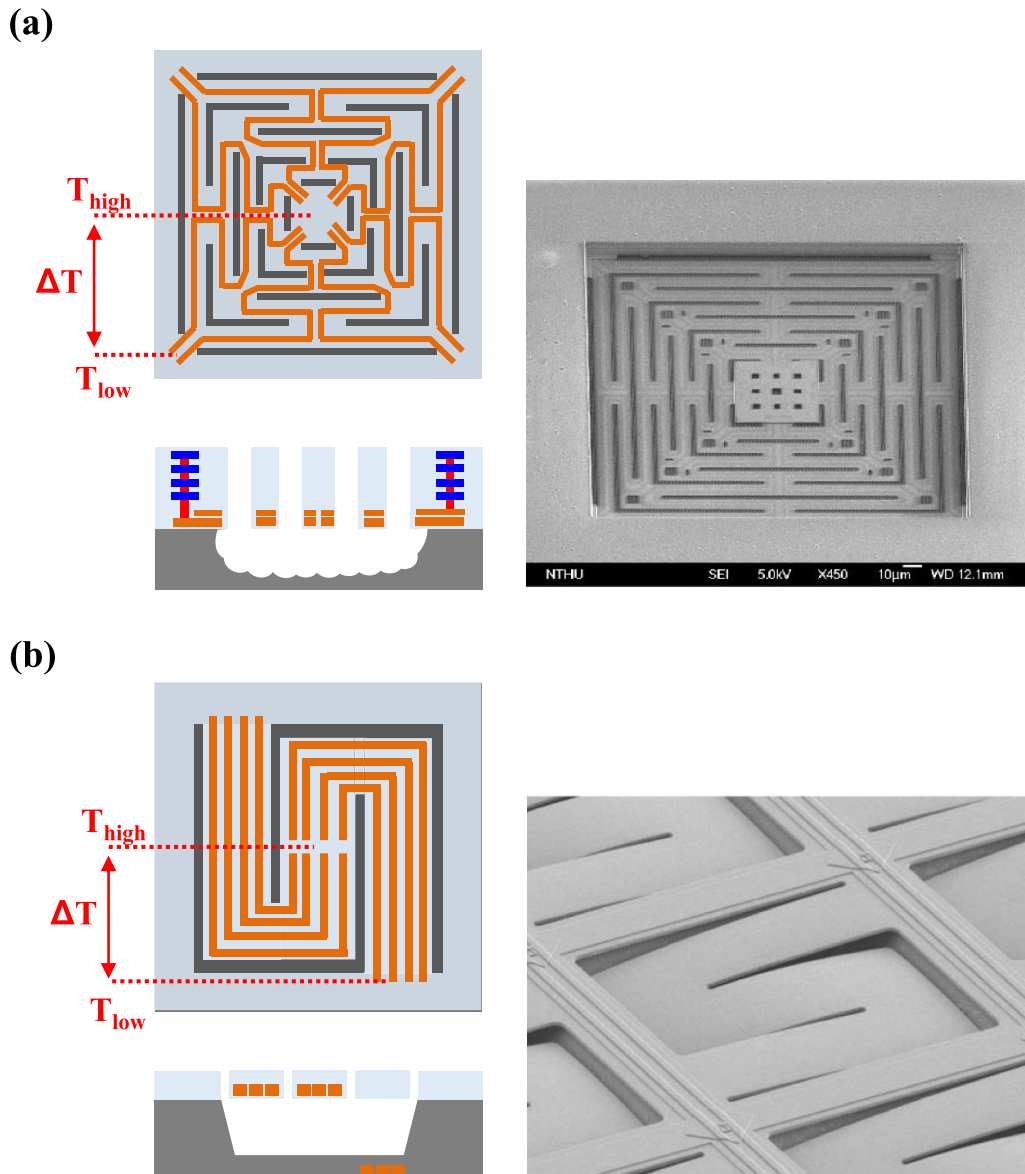


Figure 5. The schematic illustrations and SEM micrographs of serpentine structures have been designed to enhance the thermoelectric IR sensor sensing signal: (a) increase the thermal resistance between the center (T_{high}) to the boundary (T_{low}) [50]. © [2017] IEEE. Reprinted, with permission, from [50], and (b) increase the thermal resistance R_{th} and the number N of thermocouples [51]. © [2014] IEEE. Reprinted, with permission, from [51].

sensors to achieve high absorptivity and broadband absorption [53, 54]. Note that the compatibility of these materials and their related processes with existing CMOS platforms is still a concern. Moreover, various optical absorbers based on the Fabry–Pérot interference [55, 75, 76] and the metamaterial [56, 57] have been adopted by CMOS-MEMS IR sensors for absorbing IR radiation at specific wavelengths. As shown in figure 6(c), the metamaterial (featuring in micro and nano-structures designed based on the absorbing wavelength) are fabricated and vertically integrated with the serpentine plate absorber by using the TSMC 0.18 μm 1P6M process [56, 57]. With the capability of CMOS processes, the metamaterial with structures of sub-micron linewidth can be well defined. The design concepts in figure 6 to add extra materials or structures

to enhance the IR absorption can also be extended to the applications of CMOS-MEMS bolometers.

2.2. Bolometer

Figure 2(b) displays a typical bolometer type MEMS IR sensor consisted of the absorber with embedded TCR material (or diode) and the thermal-isolation structure. Similarly, the suspended absorber, supported by the thermal-isolation structures, is designed to avoid the thermal loss. As IR is incident on the sensor, the temperature of the absorber will rise, and the TCR material or diode embedded in the absorber could detect the temperature variation to determine the absorbed IR intensity. The TCR material has been employed in various

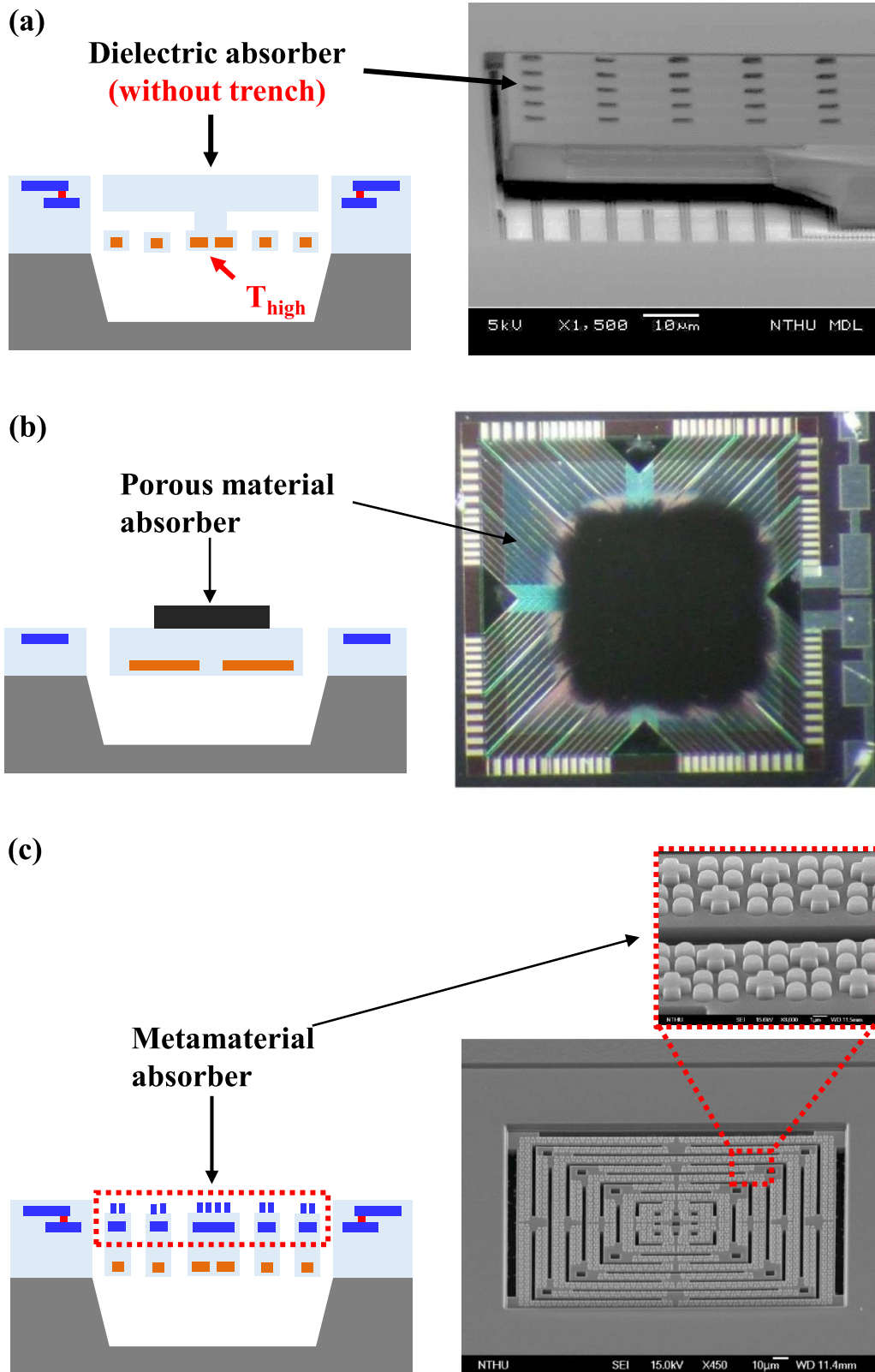


Figure 6. The schematic illustrations and SEM micrographs of the absorber material for thermoelectric IR sensor: (a) an umbrella-like structure with the serpentine plate absorber [44], Reproduced from [44]. © IOP Publishing Ltd. All rights reserved. (b) Au-black [54], © [2011] IEEE. Reprinted, with permission, from [54] and (c) metamaterial [56, 57]. © [2020] IEEE. Reprinted, with permission, from [57].

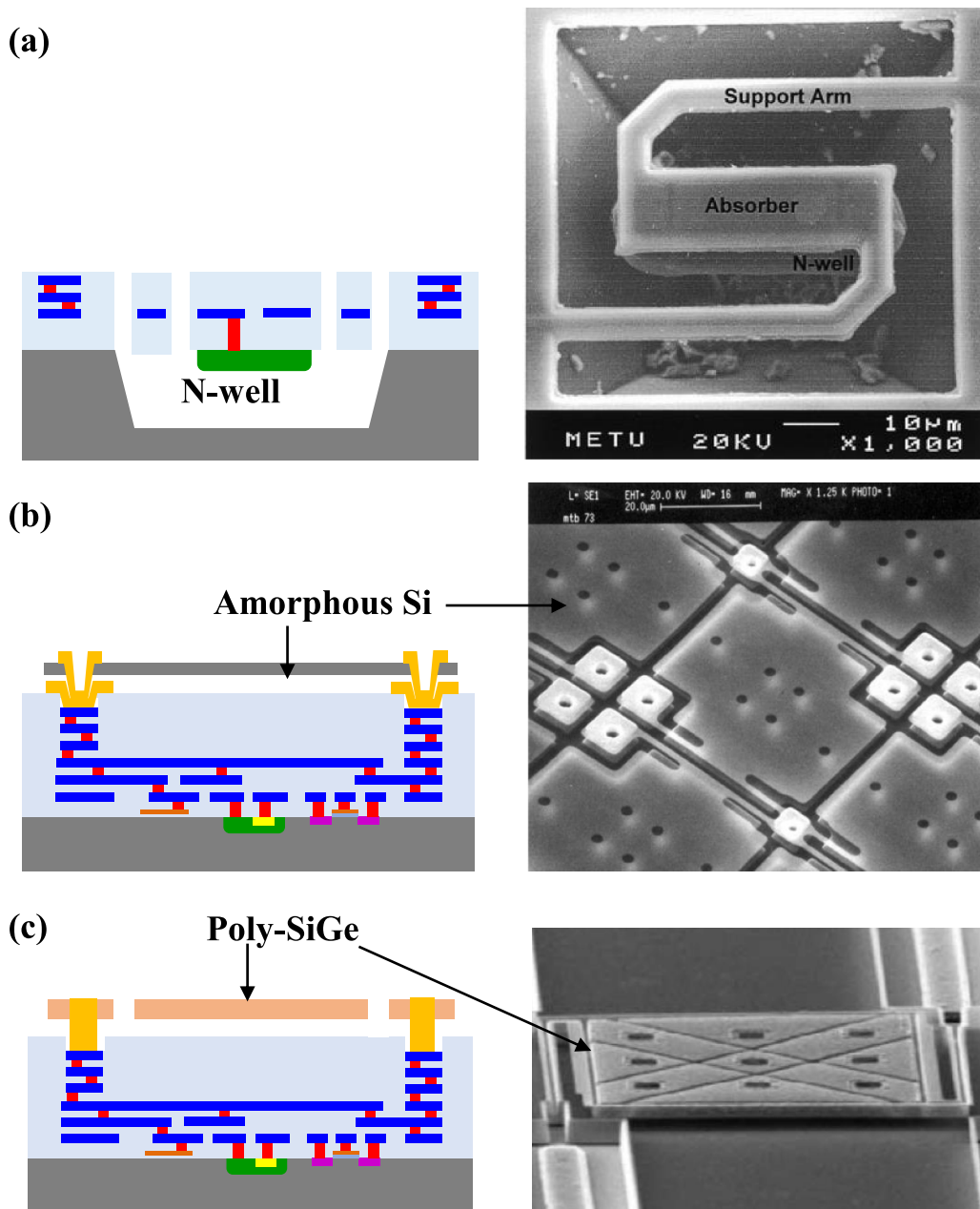


Figure 7. The schematic illustrations and SEM micrographs of the CMOS-MEMS bolometer IR sensors based on different absorber material: (a) the high TCR N-wells [59], © [2003] IEEE. Reprinted, with permission, from [59]. (b) amorphous silicon layer [60], Reprinted with permission from [60] and (c) poly-SiGe [63]. Reprinted with permission from [63].

CMOS-MEMS bolometers [59–63] to detect the temperature through the electrical resistance change. The approach to employ the voltage drop of the diode to detect temperature has also been demonstrated in CMOS-MEMS bolometers [64–66].

The metal and semiconductor films inherent in CMOS platforms exhibit the TCR effect and can be exploited to fabricate the TCR-based CMOS-MEMS bolometer [77]. As shown in figure 7(a), the high TCR N-wells (N-type diffusion done in P-type substrate) available in the CMOS platform have been exploited in [59] by the *ams* 0.8 μm CMOS process to implement the CMOS-MEMS microbolometer. The N-wells are embedded in the suspended absorber structure

made of the BEOL dielectric layers. The electrochemical etching-stop technique was employed to protect the N-wells during the post-CMOS bulk silicon etching. As depicted in figure 7(b), an additional amorphous silicon layer deposited and patterned during the post-CMOS processes was exploited by [60] to realize microbolometers on CMOS wafers. In this case, the amorphous silicon layer acts as the absorber as well as the TCR sensing material. Unlike the bulk micromachined devices shown in figure 2, an additional sacrificial layer is also required to suspend this surface micromachined sensing structure. Similar post-CMOS processes are also used to fabricate an additional vanadium oxide structure on a CMOS chip for microbolometers [58]. In addition to the conventional

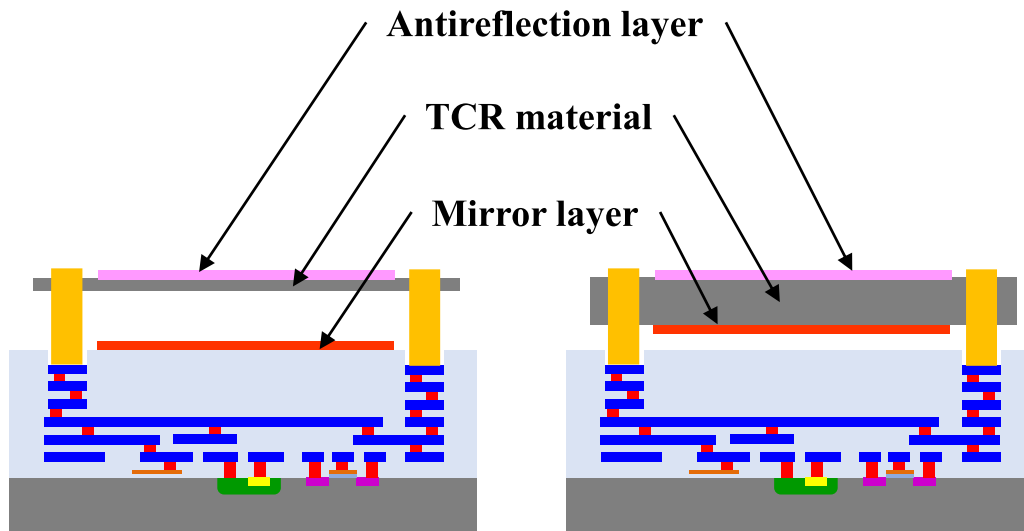


Figure 8. The schematic illustrations of the Fabry–Pérot structures (with antireflective and mirror layers) on the bolometer IR sensors.

CMOS platforms, the Ge-doped poly-Si (poly-SiGe) available in bipolar CMOS (BiCMOS) platform could offer high TCR, and hence has been employed as the temperature sensing material for CMOS-MEMS bolometers [62, 63]. As indicated in figure 7(c), the TCR-based poly-SiGe bolometer fabricated by the *imec* BiCMOS platform showed excellent performance [63]. Moreover, the surface micromachining on the CMOS chip shown in figures 7(b) and (c) has been extended to add the Fabry–Pérot structure on the bolometers to enhance the IR absorption [60, 78]. As shown in figure 8, in addition to the TCR material, additional antireflective and mirror layers were prepared for the CMOS chip in these designs.

As for the diode-based MEMS microbolometers, it is straightforward to exploit the temperature dependence of diode voltage for the measurement of absorber temperature. As shown in figure 9(a), conventional p–n diodes available in standard CMOS platforms were fabricated and integrated with the suspended absorber to implement the CMOS-MEMS microbolometers [64]. The electrochemical etching-stop technology presented in [59] is also required to protect p–n diodes during the post-CMOS bulk-silicon etching. As displayed in figure 9(b), to replace the relatively complicated electrochemical etching-stop technology, the diode-based CMOS-MEMS bolometers fabricated on the SOI wafer using the in-house CMOS processes are presented in [65, 66].

2.3. Summary

As summarized in table 1, this section reviews two different types of CMOS-MEMS IR sensors, which includes the thermoelectric and bolometric types. With the contributions of MEMS technologies, the suspended micromachined structures are realized by the post-CMOS processes to prevent the thermal loss from Si substrate. Moreover, special structure designs by using the BEOL layers of CMOS processes are achieved to enhance the IR absorption as well as the thermal resistivity of the sensor to increase the sensing signal. For the thermoelectric type sensors, the existing CMOS layers are

exploited to realize the thermocouples, whereas for the bolometer type sensors, several functional films (with high TCR) not inherent in CMOS platforms are employed to improve the performance. To further enhance the IR absorption, the large area and metamaterial absorbers have also been developed using the BEOL CMOS layers. These two additional absorbers demonstrate the advantages of CMOS processes: to equip with multi-layer thin films for flexible design, and to enable small linewidth structures for special application. In general, the suspended MEMS structures are designed for thermal isolation, and are not required to deform or move. Therefore, the potential structural deformations caused by residual stresses or the mis-match of thermal expansion coefficients can be mitigated.

3. Pressure sensors (barometers)

Pressure sensors are one of the earliest MEMS devices to be developed and commercialized. In addition to the well-known tire pressure monitoring, MEMS pressure sensors have also been developed for sensing surrounding air pressure information (or named MEMS barometer) [79–81] in a wide range of applications. For example, due to the rise in consumer electronics, pressure sensors have been integrated onto wearable devices such as smart watches [82] for measuring blood pressure [83, 84], but have also been integrated with inertial sensing units (accelerometers, gyroscopes and magnetometers) to form the indoor navigation module in mobile phones [85, 86]. Due to the advantages mentioned in the Introduction, pressure sensors developed using CMOS platforms have been heavily reported in the recent literature. Most of the reported CMOS-MEMS pressure sensors for environment monitoring are of the absolute type [87–89]. As shown in figure 10, compared to a differential pressure sensor, an absolute pressure sensor utilizes a released structure capable of deforming during pressure change, in combination with a sealed chamber that serves both as space for structural deformation, but also as a reference for detecting pressure difference. As such, two important

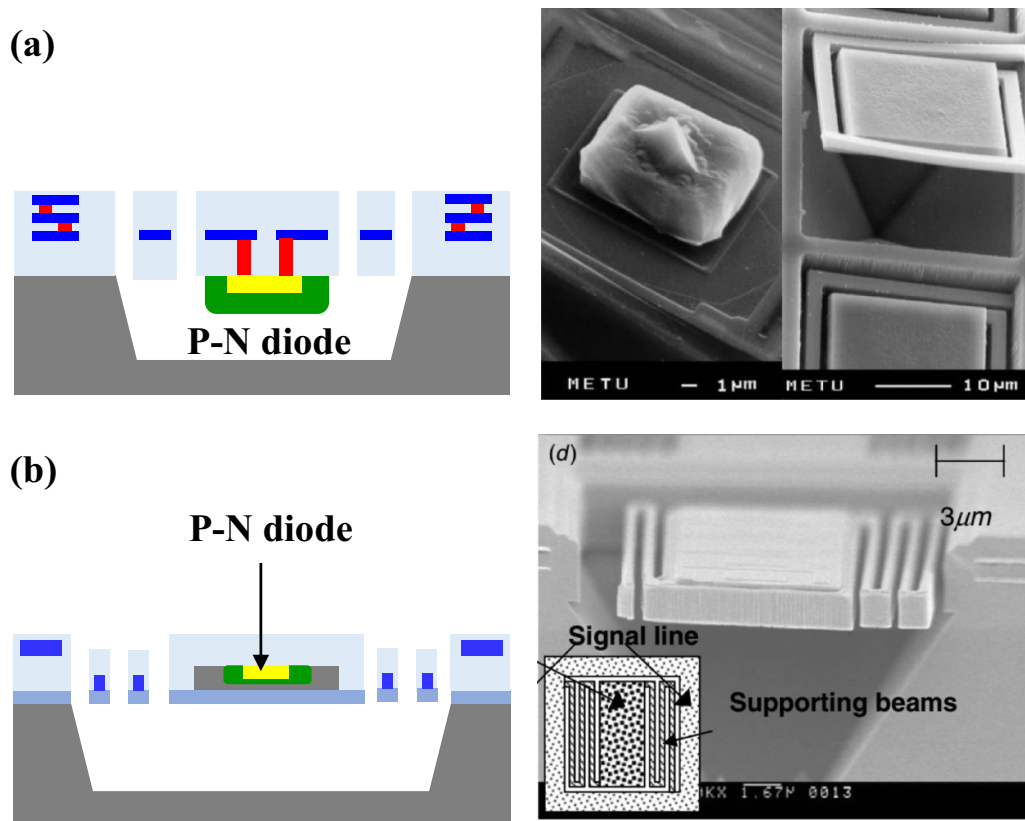


Figure 9. The schematic illustrations and SEM micrographs of the diode-based CMOS-MEMS microbolometer: (a) the p–n diodes on CMOS platform [64] © [2008] IEEE. Reprinted, with permission, from [64], and (b) the p–n diodes on SOI-CMOS platform [66]. Reproduced from [66]. © IOP Publishing Ltd. All rights reserved.

design concerns regarding absolute type CMOS-MEMS pressure sensors are the methods for fabricating the structure of the device, and the sealing of the reference pressure chamber. It is worth to note that the pressure of reference chamber is highly dependent on the sealing process. Moreover, according to the idea gas law for a sealed chamber:

$$PV = nRT, \quad (1)$$

where P , V and T are respectively the chamber pressure, volume, and temperature, n is the gas molecules amount in the sealed chamber, and R is the ideal gas constant, the chamber pressure P may vary with the temperature T , and ΔP (chamber pressure variation) is proportional with $n \times \Delta T$ (temperature change). Thus, higher vacuum condition (smaller n) in the sealed chamber could reduce the thermal drift.

The following discussions in this section will be dedicated in reviewing absolute pressure sensors fabricated using, or in combination with, the CMOS platform. The two most commonly employed sensing mechanism for pressure sensing, the capacitive and the piezoresistive type, will be separately reviewed. In addition, for the capacitive and piezoresistive sub-sections, methods for fabricating the pressure sensor structure and methods for sealing the reference pressure chamber will be discussed.

3.1. Capacitive pressure sensors

The most common mechanism for CMOS-MEMS pressure sensors is the capacitive sensing mechanism. In general, the capacitive CMOS-MEMS pressure sensor is consisted of a released flexible structure with embedded sensing electrodes, a reference sensing electrode anchor to the substrate or fixed to an undeformable structure, and the gap between the two sensing electrodes. For this sensing scheme, when a pressure load causes a deformation of the released flexible structure, the change in gap distance between two sensing electrodes (i.e. the gap-closing mechanism) will induce a capacitance variation. In this regard, the flexible structure with embedded sensing electrode and the sensing gap are important design concerns to enhance the sensitivity of the device. Various approaches to fabricate and seal the absolute type capacitive CMOS-MEMS pressure sensor will be reviewed in this sub-section.

To begin with, most reported literature on capacitive CMOS-MEMS pressure sensors is fabricated by directly using the CMOS layers of the platform in combination with deposition for sealing the pressure chamber. By this method, the released flexible structure, sensing electrodes, electrical routings, and the sensing gap of the pressure sensor can all be fabricated using the BEOL layers of the CMOS process [90]. As shown in figure 11, by performing post-CMOS metal wet etching to remove the sacrificial metal layers, the flexible structure of the pressure sensor can be successfully released. Additional

Table 1. CMOS-based infrared sensors with different sensing technique and their benefits/concerns.

Sensing type	Design/process features	Concerns	Platform	Responsivity	Detectivity/NETD	Reference
Thermoelectric	<ul style="list-style-type: none"> • Increase the absorption area • Increase the net Seebeck coefficient by removing the silicide layer (p-type: 286/n-type: -313 mV K^{-1}) • More number of thermocouples • Low electrical resistance • Etching stop by crystal plane (KOH) • High net Seebeck coefficient (P-type/N-type poly-Si) • Front-side etching • Large thermal resistance (serpentine structure) • High net Seebeck coefficient 	<ul style="list-style-type: none"> • The increase of thermal capacitance 	TSMC 0.18 μm 1P6M CMOS platform	691.5 v/w	$9 \times 10^7 \text{ cm}\sqrt{\text{Hz}}/\text{W}$	[44, 45]
	<ul style="list-style-type: none"> • More number of thermocouples • Low electrical resistance • Etching stop by crystal plane (KOH) • High net Seebeck coefficient (P-type/N-type poly-Si) • Front-side etching • Large thermal resistance (serpentine structure) • High net Seebeck coefficient 	<ul style="list-style-type: none"> • Less thermal resistance • Low net Seebeck coefficient (Al/N-type poly-Si) 	EM Microelectronic-Marin SA CMOS platform	11 v/w	$1.56 \times 10^7 \text{ cm}\sqrt{\text{Hz}}/\text{W}$	[46, 47]
	<ul style="list-style-type: none"> • High net Seebeck coefficient (P-type/N-type poly-Si) • Front-side etching • Large thermal resistance (serpentine structure) • High net Seebeck coefficient 	<ul style="list-style-type: none"> • Large electrical resistance 	AMS CMOS platform	72 v/w	$2.4 \times 10^7 \text{ cm}\sqrt{\text{Hz}}/\text{W}$	[49]
	<ul style="list-style-type: none"> • High net Seebeck coefficient 	<ul style="list-style-type: none"> • Limited number of thermocouples • Large electrical resistance • Etching time control (XeF_2) 	TSMC 0.35 μm 2P4M CMOS platform	146.4 v/w	$2.0 \times 10^6 \text{ cm}\sqrt{\text{Hz}}/\text{W}$	[50]
	<ul style="list-style-type: none"> • More number of thermocouples (256 pairs) • High net Seebeck coefficient (P-type/N-type poly-Si) • Etching stop by crystal plane (TMAH) • Smaller electrical resistance (P-type poly-Si/Au; 12–15 kΩ) • More number of thermocouples 	<ul style="list-style-type: none"> • Less thermal resistance • Large electrical resistance (100 kΩ) 	In-house CMOS process by Omron	140 v/w	N/A	[51]
	<ul style="list-style-type: none"> • Smaller electrical resistance (P-type poly-Si/Au; 12–15 kΩ) • More number of thermocouples 	<ul style="list-style-type: none"> • Low CMOS compatibility (Au) • Less thermal resistance 	In-house CMOS process by U Michigan	64 v/w	$7.0 \times 10^7 \text{ cm}\sqrt{\text{Hz}}/\text{W}$	[52]

(Continued.)

Table 1. (Continued.)

Sensing type	Design/process features	Concerns	Platform	Responsivity	Detectivity/NETD	Reference
	<ul style="list-style-type: none"> • High absorptivity • Broadband absorption • High responsivity 	<ul style="list-style-type: none"> • Low CMOS compatibility (Au) • Complicated post-processes 	N/A	3900 v/w	N/A	[53]
	<ul style="list-style-type: none"> • High absorptivity • Broadband absorption 	<ul style="list-style-type: none"> • Low CMOS compatibility (Au) • Additional mask for depositing Au-black • Process control (oblique angle of grating) 	N/A	62.8 v/w	1.88×10^8 cm $\sqrt{\text{Hz}}/\text{W}$	[54]
	<ul style="list-style-type: none"> • Polarization-dependent sensitivity (for polarimetric IR imaging) • Tunable absorption spectrum • Absorptivity enhancement (20%) • High CMOS compatibility • Single crystal Si thermocouple 	<ul style="list-style-type: none"> • Time-controlling etching 	TSMC 0.18 μm 1P6M CMOS platform	92.17 v/w	6.13×10^8 cm $\sqrt{\text{Hz}}/\text{W}$	[56, 57]
		<ul style="list-style-type: none"> • High cost • Additional lithography (back-side etching) • Complex micromachining process (electrochemical etching-stop technique) • Lower TCR value (0.24%/K) 	In-house SOI-CMOS process by Cambridge CMOS sensors	23 v/w	7.5×10^7 cm $\sqrt{\text{Hz}}/\text{W}$	[68]
Bolometer	<ul style="list-style-type: none"> • No additional lithography and deposition of sensing material (CMOS N-well layer serves as sensing material) • Low cost (minimal post-processes) • Low 1/f noise 		AMS 0.8 μm CMOS platform	2000 v/w	2.6×10^8 cm $\sqrt{\text{Hz}}/\text{W}$	[59]

(Continued.)

Table 1. (Continued.)

Sensing type	Design/process features	Concerns	Platform	Responsivity	Detectivity/NETD	Reference
	<ul style="list-style-type: none"> • Excellent TCR value (amorphous Si; 2.5–5%/K) • Simple post-process (conventional surface micromachining technique) • High CMOS compatibility • Excellent TCR value (VO_x); • Simple post-process (conventional surface micromachining technique) • High CMOS compatibility (compared with Amorphous Si and VO_x) • Uniformity of resistance and TCR 	<ul style="list-style-type: none"> • Additional lithography and thin-film deposition during post processes • High $1/f$ noise (due to crystal quality) • Additional lithography and thin-film deposition during post processes • High $1/f$ noise (due to crystal quality) • Larger size (compared with Amorphous Si and VO_x) • Higher $1/f$ noise 	In-house CMOS process by CEA-Leti	N/A	N/A	[60]
			0.18 μm CMOS process	N/A	$< 3 \times 10^{-2}$ K	[61]
			imec BiCMOS platform	200 v/w	8×10^{-2} K	[63]
Diode	<ul style="list-style-type: none"> • Low cost • Low noise (under low bias current) • No additional lithography and deposition of sensing material (CMOS p–n diode) • Simple post-process (conventional bulk-micromachining technique) • Low $1/f$ noise • Stable electrical and thermal characteristics 	<ul style="list-style-type: none"> • Complex micromachining process (electrochemical etching-stop technique) • High cost (SOI-CMOS) 	AMS 0.35 μm CMOS platform	4970 v/w	10^3 K	[64]
			In-house SOI-CMOS process by Mitsubishi Electric Corporation	9.3×10^{-4} v/w	0.12 K	[65, 66]
			In-house SOI-CMOS process by Toshiba Corporate Research and Development Center			

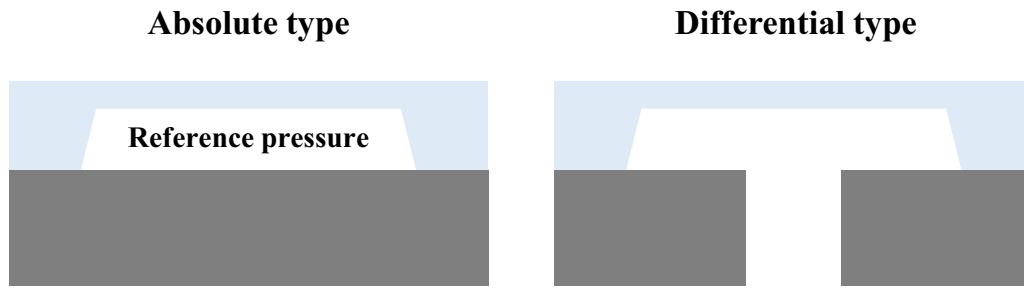


Figure 10. The schematic illustrations of MEMS pressure sensors (barometers): (a) absolute type and (b) differential type.

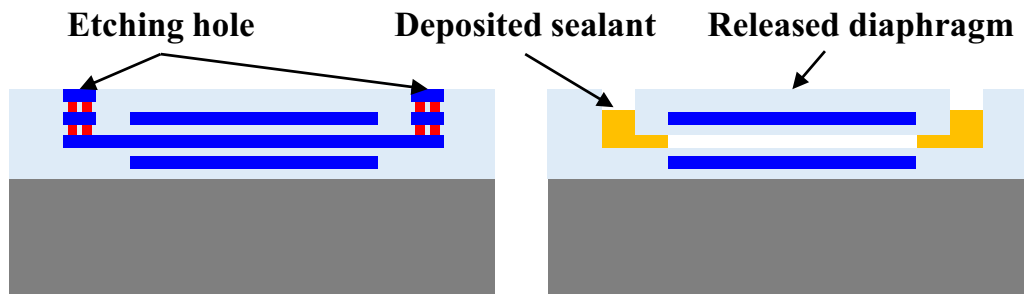


Figure 11. The schematic illustrations of the post-CMOS metal wet etching for sub-micro sensing gap fabrication and sealing chamber by sealant.

structural designs may also be incorporated through the use of multiple sacrificial metal layers and the connecting tungsten vias. Moreover, the sub-micron level sensing gap can be achieved through this approach to enhance the sensitivity of the capacitive pressure sensor. As indicated in figure 11, the sealant is used to seal these pressure sensors, and different films, for example parylene, metals or other materials, can be deposited [87–96]. Note that the vacuum condition of the sealed chamber is determined by the pressure of film deposition chamber (for example: the chamber pressure is near 10 Pa (~ 75 mTorr) if sealed by the parylene [87–89]) and the outgassing from chamber walls during subsequent processes.

In [91], a capacitive pressure sensor integrated with a ring oscillator circuit was investigated, as shown in figure 12(a). The device was fabricated using the *TSMC* 0.35 μm CMOS process combined with in-house sacrificial layer etching to release the flexible circular diaphragm with embedded sensing electrode. The fabrication process was completed by sealing the reference chamber using parylene. The ring oscillator was integrated with the sensing device to convert the capacitance signal into a frequency output. Using a similar approach, the pressure sensor from a commercial 0.35 μm 2P4M process in [92] was fabricated and also sealed with parylene. The pressure sensor was integrated, on-chip, with a reference capacitor and readout circuitry to form a fully differential readout circuit. Similar fabrication and sealing processes by parylene were also reported in [87–89], and additional structural designs were incorporated using the BEOL layers of the *TSMC* 0.18 μm 1P6M CMOS process to enhance the performance of the pressure sensors. In [87], a double deformable diaphragm structure was presented, which was realized by releasing the fixed electrode to allow for deformation, as

shown in figure 12(b). This design enables a larger gap distance change between the two deformable sensing electrodes during pressure loadings. This design was shown to effectively enhance the sensitivity of the sensor by 2.9-fold. Furthermore, a CMOS-MEMS corrugated diaphragm was reported in [88], as shown in figure 12(c). Corrugated structures have been utilized in various devices to reduce the influence of thin film residual stress for performance improvement [97–99]. Therefore, novel layers stacking design was proposed in [88] to implement the corrugated diaphragm to enhance the sensitivity performance of the pressure sensor by reducing the residual stress influence of the CMOS platform. Measurement results show a near 5-fold enhancement in sensitivity and an effective release of diaphragm residual stress. Lastly in [89], a mechanical force-displacement transduction structure was designed to enhance the sensitivity performance, as shown in figure 12(d). The mechanical force-displacement design was also defined using the CMOS BEOL layers. The released sensing electrode was supported by the deformable diaphragm above through a connecting pillar. This design could avoid the deformation of sensing electrode during pressure loadings to increase the sensing capacitance. By using the CMOS platform and parylene deposition, absolute type capacitive pressure sensors have been successfully realized with dedicated circuitry for sensing, or with novel structural design for performance enhancement.

Other than using parylene for sealing the absolute pressure sensor chamber, materials such as metal or other materials can also be used, as shown in figure 13. As shown in figures 13(a) and (b), pressure sensor fabricated from the *SMIC* 0.18 μm CMOS process was sealed using evaporated aluminum [93]. The deformable structure of the pressure sensor was also

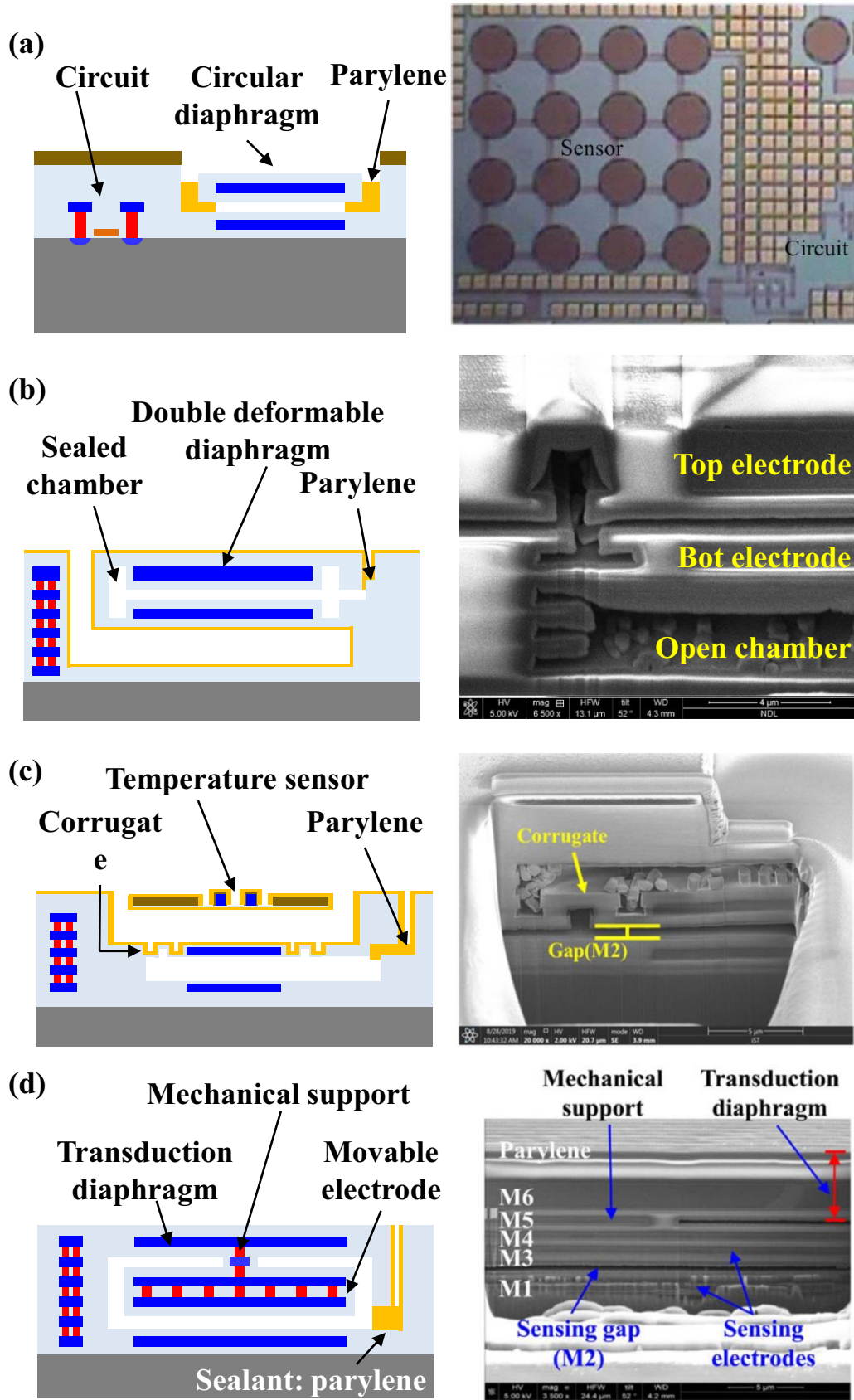


Figure 12. The schematic illustrations and SEM micrographs of the sealing processes by parylene: (a) the flexible circular diaphragm structure [91], Reproduced from [91]. CC BY 3.0. (b) The double deformable diaphragm structure [87], © [2020] IEEE. Reprinted, with permission, from [87]. (c) The corrugated diaphragm structure [88]. © [2017] IEEE. Reprinted, with permission, from [88] and (d) mechanical force–displacement transduction structure [89]. Reproduced from [89]. © IOP Publishing Ltd. All rights reserved.

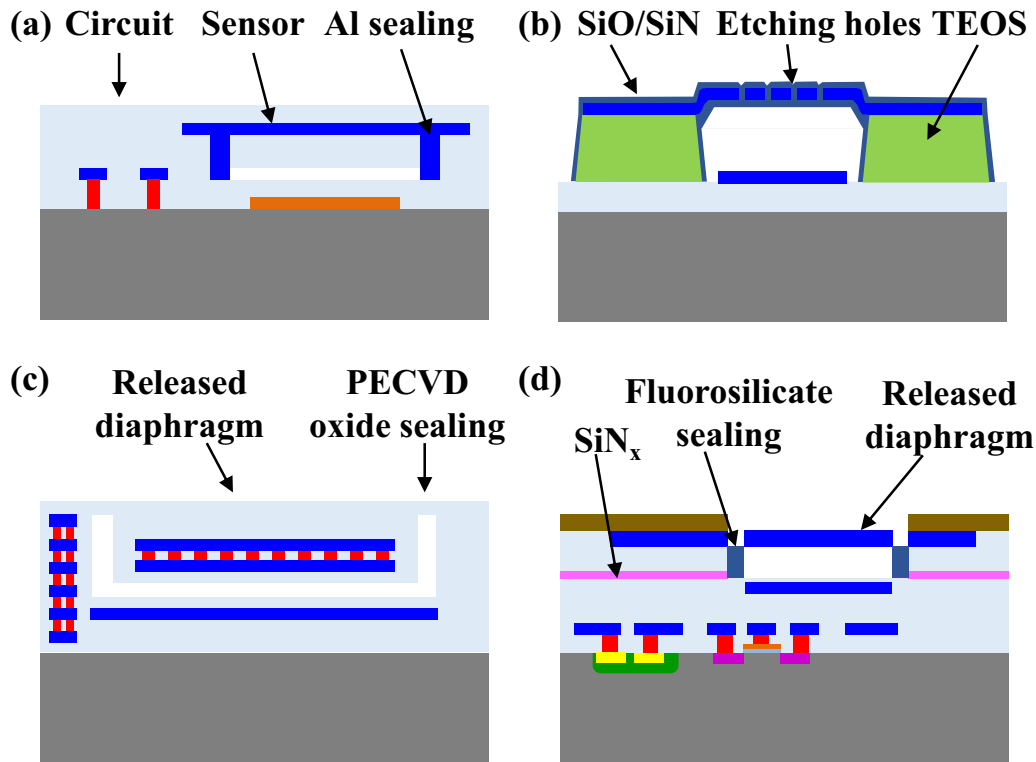


Figure 13. The schematic illustrations of the absolute pressure sensor sealed by depositing various materials: (a) Al [93], (b) TEOS [94], (c) silicon dioxide [95] and fluorosilicate glass [96].

released by the post-CMOS sacrificial layer etching. It should be noted that the sealing process (by evaporated Al) simultaneously serves to form the top sensing electrode of the capacitive pressure sensor, and the reference chamber pressure could reach $4\text{--}8 \times 10^{-6}$ Torr. The pressure sensor is integrated, on-chip, with an interface circuit for capacitance-to-digital conversion for passive radio frequency identification (RFID) applications. Furthermore, as shown in figure 13(b), the sensor was implemented using the in-house CMOS and post-CMOS processes, and the chamber was sealed using deposited tetraethyl orthosilicate (TEOS) oxide with a pressure of 0.4–0.5 Torr [94]. Similarly, using the CMOS BEOL to define the pressure sensor structure [95, 96], have demonstrated the sealing of the reference chamber using materials such as silicon dioxide (with a chamber pressure of 6 mTorr) and fluorosilicate glass (with a chamber pressure of 0.5 Torr), both by the PECVD (plasma-enhanced chemical vapor deposition) process, respectively shown in figure 13(c) and (d). The CMOS processes used to define the pressure sensor structure [95, 96] were respectively the **GLOBAL-FOUNDRIES** (GlobalFoundries Inc., USA) 0.18 μm CMOS process, and the 8 M 130 nm **IBM** (International Business Machines Corp., USA) CMOS process.

From the previous literature, it can be seen that many absolute CMOS-MEMS pressure sensors are fabricated through the etching of CMOS layers, and sealed by depositing various different materials. In fact, the wafer bonding approaches, as shown in figure 14, offer a simple solution to fabricate absolute

CMOS-MEMS pressure sensors. In [100] (figure 14(a)), the structure of the pressure sensor was defined using the inherent thin films of the **TSMC** 2P4M CMOS process. For post-CMOS processes, the deep reactive ion etching (DRIE) process was first used to back-side etch the silicon substrate of CMOS chip, followed by the sensing diaphragm definition using the metal wet etching. Thus, sensors of different sensitivity and sensing range can be achieved by varying the stacking of metal and dielectric layers. This is the advantage contributed by the multi-layers CMOS process. Although the vacuum sealing is not demonstrated in [100], it is straightforward to realize the absolute pressure sensor when performing the wafer bonding in vacuum chamber. The combination of using silicon bulk etching with bonding process to form the absolute CMOS-MEMS pressure sensor was demonstrated in [101]. In this study, the CMOS circuitry and structurally-defined pressure sensing diaphragm were fabricated using the CMOS process on a silicon wafer. Then, the etched silicon wafer was (flip-chip) bonded onto a glass wafer with cavity, as shown in figure 14(b). The cavity on glass could ensure a better vacuum sealing of the two bonded wafers. Moreover, the backside silicon etch was used to release the sensing diaphragm. These two studies show two different process technologies to fabricate CMOS-MEMS pressure sensors: the bonding process rather than deposition process was used to form the reference pressure chamber; the backside silicon etching rather than sacrificial layer etching was used to release the structures.

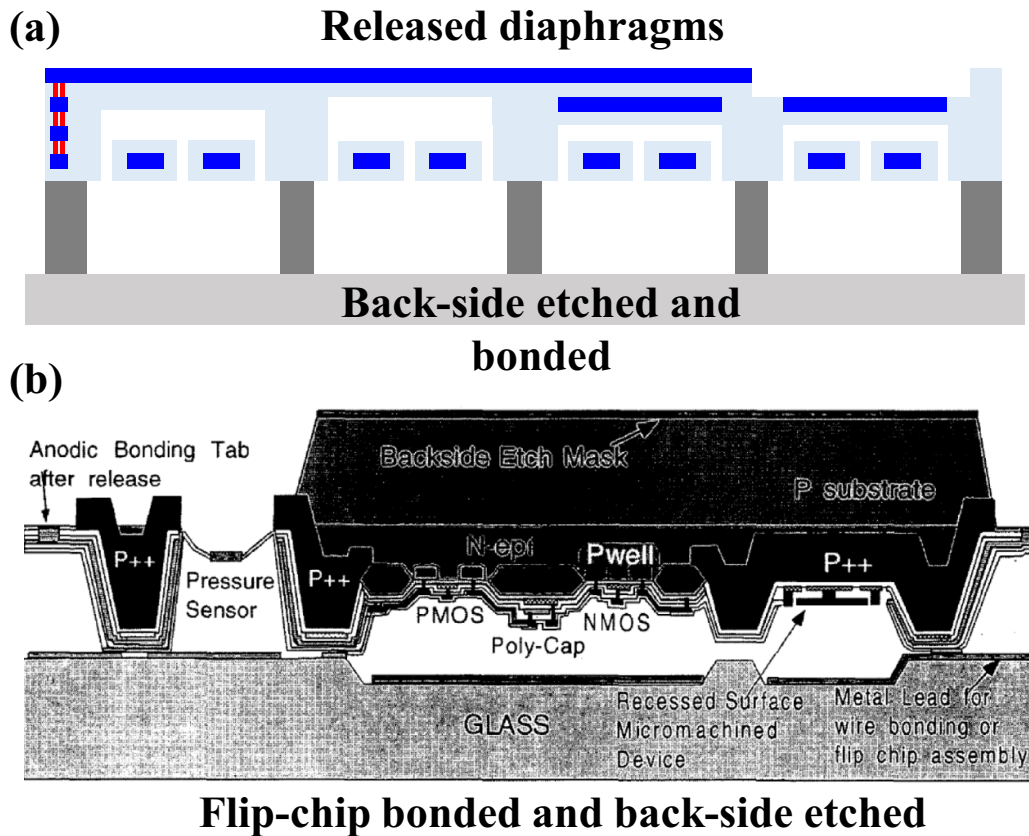


Figure 14. The schematic illustrations of the absolute pressure sensor sealed by bonding technique: (a) bonding with Pyrex glass [100] and (b) anodic bonding [101]. (b) © [2002] IEEE. Reprinted, with permission, from [101].

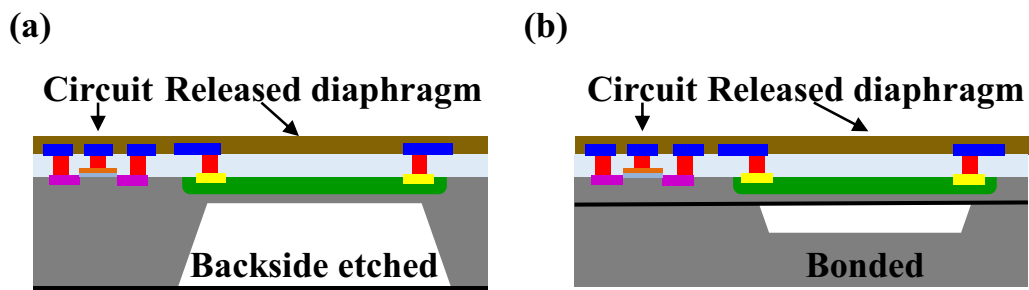


Figure 15. The schematic illustrations of the piezoresistive pressure sensors: (a) the backside and (b) front side Si bulk micromachining.

3.2. Piezoresistive pressure sensors

Another sensing mechanism employed for CMOS-MEMS pressure sensor is the piezoresistive type mechanism. The inherent poly-Si layers in CMOS platforms exhibit reasonable gauge factor [102], and hence could be adopted as the sensing material to realize the CMOS-MEMS piezoresistive pressure sensors. By using the available CMOS layers combined with post-CMOS processes such as sacrificial layers etching, and bulk silicon etching, the deformable suspended structures with embedded piezoresistive (poly-Si) films can be fabricated. The piezoresistive type pressure sensor is realized after the CMOS-MEMS chip is bonded to seal the pressure chamber. As the suspended CMOS-MEMS structure deformed by the pressure load, the resistance of the embedded poly-Si will be changed.

Thus, the pressure is detected by the induced resistance change of the piezoresistive material.

The conventional process technologies to fabricate micro piezoresistive pressure sensors on Si substrate using bulk micromachining and bonding [103] can be applied to implement counterparts on a CMOS wafer [104, 105]. As shown in figure 15(a), the backside Si bulk micromachining is performed on the CMOS chip (with sensing circuits, poly-Si piezoresistors, and electrical routings prepared by CMOS processes) to define the thickness of the deformable diaphragm for pressure sensor. Note bonding process is required to form the reference pressure chamber. The concept has been demonstrated in [104] by adopting the 0.6 μm standard CMOS process from *ams* foundry to implement the piezoresistive CMOS-MEMS pressure sensors with circuitry. Another

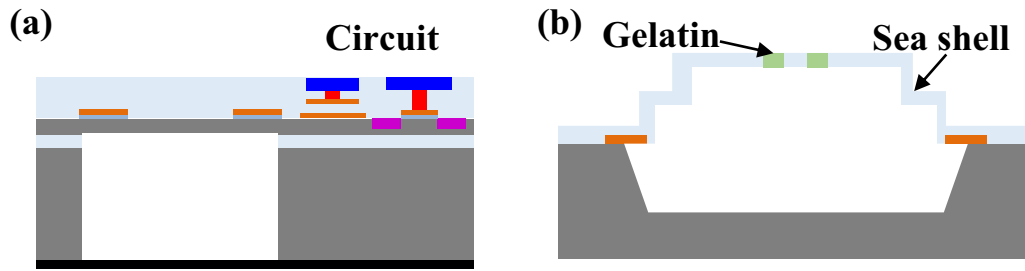


Figure 16. The schematic illustrations of the piezoresistive pressure sensors by different structure and platform: (a) clamped membranes and (b) seashell diaphragm.

approach is shown in figure 15(b), where the CMOS chip (including sensing circuits, poly-Si piezoresistors, and electrical routings prepared by the CMOS processes) was carried out on a thinned Si wafer (to achieve appropriate diaphragm thickness) that is bonded to another Si wafer (with bulk micromachined cavity) to realize the pressure sensor. In this case, the bonding process is used to avoid a large cavity on pressure sensing chip [105]. The bonding of the two wafers will complete the sealing of the reference pressure chamber. As reported in [105], the *X-FAB* 1.0 μm CMOS platform has been exploited to demonstrate the CMOS-MEMS piezoresistive pressure sensor shown in figure 15(b).

In addition to the bulk Si micromachining on CMOS chip, the CMOS-MEMS piezoresistive pressure sensors have also been implemented using different approaches [106, 107]. In [106], a CMOS-MEMS piezoresistive pressure sensor integrated with on-chip sensing circuit fabricated using the *Semfab* 2P1M CMOS process on SOI wafer was reported, as shown in figure 16(a). The deformable membrane of the pressure sensor is fabricated using the device silicon layer of SOI wafer; and the poly-Si layers of the CMOS process act as the piezoresistive sensing material. The structure is released from substrate by backside DRIE, and the reference chamber can be achieved after the bonding. Moreover, the CMOS layers can also be directly used as sacrificial layers to release the deformable structure [107]. As displayed in figure 16(b), after combining the etching of sacrificial metal layers and bulk Si, the ‘seashell’ diaphragm design can be achieved to reduce its stiffness to enhance the sensitivity of CMOS-MEMS piezoresistive pressure sensor. Note that gelatin is used to seal the etching release holes on diaphragm, yet the sealing process remains a concern for this design. Thus, the thin film deposition to seal the reference pressure chamber is required to realize the absolute pressure sensor.

3.3. Summary

Numerous different types of CMOS-MEMS pressure sensors were reviewed in this section, as summarized in table 2. By exploiting the BEOL layers of CMOS processes, including metal, dielectric, and poly-Si films, various CMOS-MEMS capacitive and piezoresistive pressure sensors have been demonstrated. In addition to following the design rules and employing the inherent materials in the standard CMOS processes, these studies also develop novel post-CMOS processes

to fabricate different CMOS-MEMS pressure sensors. For example, the pressure sensors with different flexible deformable structures such as the circular, rectangular, corrugated, and various capacitive sensing schemes such as the single and dual deformable plates with embedded sensing electrodes and so on are also demonstrated. Moreover, the pressure sensors used for environmental sensing are typically the absolute type pressure sensor, and hence the wafer bonding or thin film (parylene, metals, silicon dioxide, etc) deposition processes were demonstrated to seal the reference pressure chamber. It is worth to note the CMOS process is a promising approach to realize the capacitive type pressure sensors since the sub-micron gaps for capacitive sensing and multi-layers for complicated electrical routings can be achieved. On the other hand, due to the constraint of the location of the available piezoresistive material in the CMOS platform, it is vital to incorporate front-side/back-side silicon bulk etching and/or bonding processes to release the pressure sensing diaphragm. The CMOS-MEMS pressure sensor of different sensing mechanisms, such as the magnetoresistive type, can also be achieved by depositing other functional materials [108].

4. Humidity sensor and temperature sensor

Humidity sensors can convert surrounding humidity information into electrical signals. Most reported literature and commercial humidity sensors measure relative humidity, which is the ratio of the actual vapor pressure of air to the saturation vapor pressure under a certain temperature. Due to the fact that the saturation vapor pressure of water is a function of temperature, relative humidity sensing will be affected by temperature [109]. As such, in application, the temperature information is a necessity to properly determine the relative humidity. To date, the commercially available conventional humidity sensor is either made with a dry-wet bulb temperature sensor or the hair tension transducer which can stretch and shrink upon humidity level changes [110]. Despite their ease of manufacture and availability on the market, conventional sensors are bulky and imprecise, limiting their adoption for wider applications. Therefore, various MEMS technologies have also been investigated and developed to design and fabricate micro humidity sensors. The sensing mechanisms include resistive type [111–113], capacitive type [88, 109, 114–124], piezo-resistive type [125] and resonance type [126, 127], etc.

Table 2. CMOS-based pressure sensors with different sensing technique and their benefits/concerns.

Sensing type	Design/process features	Concerns	Sealant	Platform	Sensitivity	Sensing range	Reference
Capacitive	<ul style="list-style-type: none"> • Larger sensing gap distance (double deformable diaphragm) • Reduced stiffness of membrane by trenches structure • Corrugated structure (inhibited residual stress, Increased sensitivity) • CMOS-BEOL process • Mechanical force-displacement transduction • High linearity by two metal layers electrode • CMOS-BEOL process • Lower parasitic effects • Elliptic structure • Varying the stacking of layers (tuning sensing range and sensitivity) • Bulk micromachining by DRIE • Bulk micromachining by EDP 	<ul style="list-style-type: none"> • Residual stress of CMOS layers • Thermal deflections • Stiction effects by metal wet-etching 	Parylene	TSMC 0.18 μm 1P6M	0.26 fF/kPa	20–110 kPa	[87]
	<ul style="list-style-type: none"> • High linearity by two metal layers electrode 		Parylene	TSMC 0.18 μm 1P6M	0.969 fF/kPa	20–120 kPa	[88]
	<ul style="list-style-type: none"> • Mechanical force-displacement transduction 		Parylene	TSMC 0.18 μm 1P6M	0.43 fF/kPa	20–300 kPa	[89]
	<ul style="list-style-type: none"> • Stiffness of membrane 		PECVD silicon dioxide	GLOBAL-FOUNDRIES 0.18 μm	0.14 fF/kPa	0–300 kPa	[95]
	<ul style="list-style-type: none"> • Complicated lithography during post processes 		PECVD fluorosilicate glass	IBM 0.13 μm	0.4 fF hPa ⁻¹ (Elliptic) 0.29 fF hPa ⁻¹ (Rectangular)	40–80 hPa	[96]
	<ul style="list-style-type: none"> • Residual stress of CMOS layers • Thermal deflections • Stiction effects by metal wet-etching 		Bonding (glass)	TSMC 0.35 μm 2P4M	0.14–7.87 mV/kPa	0–20 kPa	[100]
	<ul style="list-style-type: none"> • Bulk micromachining by DRIE • Bulk micromachining by EDP 		Flip-chip bonding (glass)	2P2M	48.8 mV/Torr	500–800 Torr	[101]

(Continued.)

Table 2. (Continued.)

Sensing type	Design/process features	Concerns	Sealant	Platform	Sensitivity	Sensing range	Reference
Piezoresistive	<ul style="list-style-type: none"> • Bulk micromachining • Good linearity • Large output • Readout circuit (Wheatstone bridge) 	<ul style="list-style-type: none"> • N/A 	Fusion bonding Anodic bonding	X-FAB 1.0 μm	(Wafer bonding) 9.4 mV/(V \times bar) 6.2 mV/(V \times bar) 2.2 mV/(V \times bar) (Bulk micromachining) 43 mV/(V \times bar) 18 mV/(V \times bar) 3.9 mV/(V \times bar) 2.4 mV/(V \times bar) 1.3 mV/(V \times bar) 8.7 mV/fbar	(Wafer bonding) 0–3 bar 0–6 bar 0–15 bar (Bulk micromachining) 0–0.5 bar 0–1 bar 0–6 bar 0–10 bar 0–15 bar 0–5 bar	[105]
		<ul style="list-style-type: none"> • High cost (SOI-CMOS) • High cost (Double-sided DRIE, etching stop by SiO₂) • Complicated etching hole design (Seashell-like diaphragm) 	2-Stage (BCB and anodic bonding)	Seme fab 2P1M			[106]
		<ul style="list-style-type: none"> • Additional Magnetic films geometry (CoFeB) deposition during post processes 	Gelatin	TSMC 0.35 μm 2P4M	8.56 \pm 0.13 mV/V/psi	0–55 psi	[107]
Magnetostrictive	<ul style="list-style-type: none"> • Planar inductors • CMOS sub-micron level layers (sensing coil turns) 		Bonding (PCB)	TSMC 0.18 μm 1P6M	0.079%/kPa	–100–300 kPa	[108]

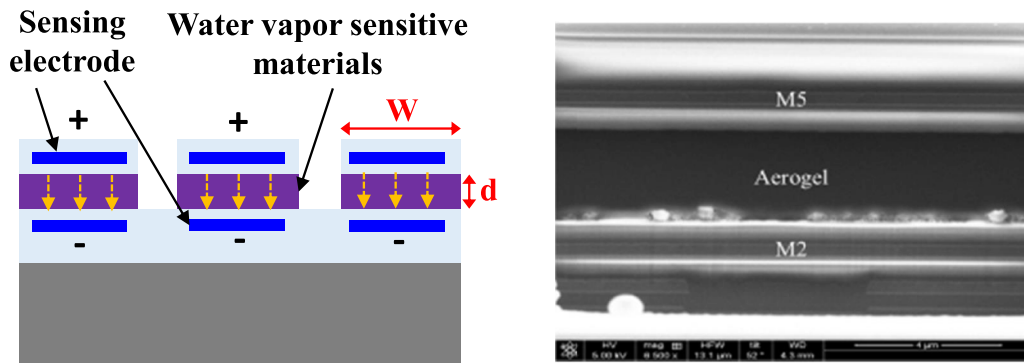


Figure 17. The schematic illustrations and SEM micrographs of MEMS humidity sensor [118]. © [2014] IEEE. Reprinted, with permission, from [118].

This section will review the CMOS-MEMS humidity sensors and their monolithic integration with thermometer as well. The basic structure of a CMOS-MEMS humidity sensor includes the water vapor sensitive materials that absorb external water vapor combined with a specially designed sensing structure. Various CMOS process platforms combined with appropriate post-CMOS fabrication techniques have been exploited to realize resistive type [113], capacitive type [116–124], and resonant type [126, 127] humidity sensors. Due to the advantages of multi-layer stacking and submicron level linewidths of CMOS processes, the CMOS-MEMS approach has been most commonly utilized to fabricate capacitive type humidity sensors. Additionally, a more comprehensive measurement of relative humidity sensor by integrating the humidity sensor with temperature sensor on a single chip can be achieved by the CMOS-MEMS technologies [88, 117, 122]. The following sub-sections will focus on capacitive humidity sensors of different sensing materials and structures design [116–124], and also provide a brief review for the CMOS-MEMS resistive [113] and resonant [126, 127] type humidity sensors.

4.1. Capacitive

Figure 17 displays a typical capacitive humidity sensor consisted of sensing electrodes and sensing material. In general, the sensing material will absorb water vapor which will further change its dielectric constant. Thus, the humidity can be detected by the capacitance change of sensing electrodes. By exploiting the existing BEOL thin film layers of the CMOS processes and design rules of the CMOS processes, different sensing electrodes can be designed and fabricated using post-CMOS processes, and then the water vapor sensing materials can be filled into the sensing electrodes. Generally speaking, the design concerns for humidity sensors may include the response time, and sensitivity [109, 111–127], etc. The response time indicates how fast the sensor can detect two different humidity levels. As a result, different sensing-electrode designs and water vapor sensing materials are developed to enhance the performances (i.e. response time, sensitivity, etc) of capacitive humidity sensors. This sub-section will review

the articles concerning the sensing materials first, and then the design of sensing electrode structures.

4.1.1. Water vapor sensing material. Since polyimide is a compatible material for the CMOS process, it is one of most common sensing material for CMOS-MEMS capacitive humidity sensors [88, 116, 117, 120–123]. Polyimide can absorb water vapor due to its morphological structure [128]. Since the dielectric constant of polyimide before and after water vapor absorption will drastically change, the output capacitance signal of the humidity sensor will vary with the level of water vapor absorbed by the polyimide [109]. However, as mentioned in [128], the diffusivity of water through polyimide will be heavily influenced by fabrication conditions and functional groups. Different methods for filling the polyimide have been demonstrated, for example by using dispensing [88, 116, 117, 121, 122], or by wafer level coating [120, 123]. In addition to polyimide, other water vapor sensing materials have been investigated due to their better diffusion coefficients or hygroscopic nanostructures, for example the RF-aerogel [118, 119], and the polypyrrole [124]. In [118, 119], RF-aerogel is an alternative water vapor sensitive polymer that exhibits high porosity, and as [124] reported, polypyrrole also has porous nanostructure. Therefore, both materials could accelerate the absorption of water vapor to enhance the response time of humidity sensors. Furthermore, RF-aerogel has a low dielectric constant, which could provide higher capacitance changes upon water vapor absorption/desorption [118, 119]. However, different drawbacks for these materials limit their wider use in CMOS-MEMS humidity sensors. For instance, even though the RF-aerogel has a better water diffusivity performance compared to the commonly used polyimide, it is relatively harder to prepare, due to the need for the sol-gel method and supercritical fluid drying during preparation [118].

4.1.2. Sensing electrode structure. As mentioned, combined with appropriate post-CMOS fabrication techniques, various high-performing sensing electrode structure designs for capacitive type CMOS-MEMS humidity sensors can be implemented using the available metal layers of the CMOS

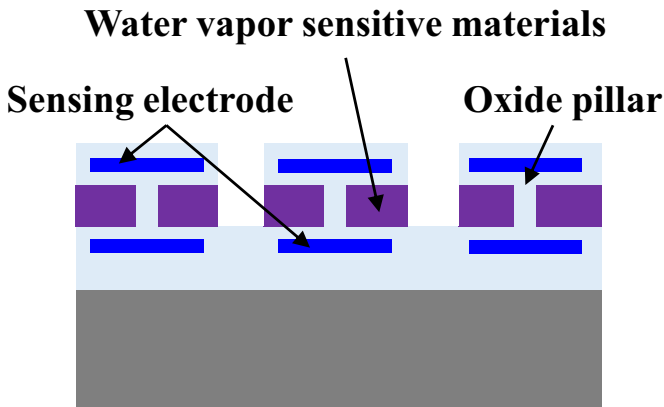


Figure 18. The schematic illustrations of the oxide pillars structure in the humidity sensors.

platform. The first common electrode structure design is the vertical parallel plate (VPP) design [116–119], as shown in figure 17. The VPP electrodes are implemented by removing one or two sacrificial metal layers, by which the space between the two out-of-plane parallel plates can be fabricated. The CMOS platform could offer two advantages for this design. Firstly, a small (sub-micron) sensing gap between VPP electrodes can be achieved by using the CMOS platform to enhance the sensitivity of capacitive humidity sensors. Secondly, the sensing area and electrical routings needed for this design can be accomplished through the metal layers of the CMOS platform. However, due to the thin film residual stresses of the CMOS-platform, warpage of the released electrode may potentially occur [129, 130]. To compensate this problem, supporting oxide pillar structures were used to enhance structural rigidity of the suspended electrodes [116–119], as shown in figure 18. Besides, the aspect ratio of the gap (W/d in figure 17) for VPP electrodes must be considered to properly fill in the water vapor sensitive materials [116–119].

The second commonly employed electrode structure design for the capacitive CMOS-MEMS humidity sensor is the interdigitated electrode (IDE), as displayed in figure 19(a). Figure 19(b) depicts the cross-section of a typical IDE humidity sensor. In this design, the sensing material is deposited on the CMOS chip with patterned metal electrodes to detect humidity via fringe capacitance change [123], as indicated by dashed lines in the figure. Figure 19(c) shows another typical design based on the IDE architecture. In this design, the parallel electrodes consisted of the CMOS BEOL metal layers and via were patterned after removing sacrificial layers during post-CMOS processes. After that, the sensing material was filled into the gap between parallel electrodes to implement the sensor [120–122, 124]. Compared with the VPP design, such IDE electrodes have a more direct filling path for water vapor sensitive material, and since no released structures are required, the issue of residual stresses of the CMOS-platform can be minimized. To pursue a faster response time for the design in figure 19(c), the use of front side silicon substrate etching [121] and double side post-CMOS processes [122]

have been demonstrated. As shown in figure 20, after the IDE is defined by dielectric layer etching, the silicon substrate was removed by DRIE and isotropic etching to release the electrodes [121]. This enables the vapor to diffuse from the top, as well as the bottom of the sensing electrode, effectively enhancing the response time of the sensor. As shown in the cross section view in figure 21, the similar concept to reduce the response time has been adopted by the humidity sensor fabricated using a double side post-CMOS etching processes [122].

Moreover, as demonstrated in [117], the post-CMOS micromachining on a CMOS chip prepared by the *TSMC* 0.18 μm 1P6M processes could be exploited to integrate a resistive-type temperature sensor and a humidity sensor with VPP sensing electrodes for relative humidity measurement. The same CMOS platform could also be leveraged to fabricate and integrate a diode-type temperature sensor with the IDE sensing electrodes humidity sensor in [122], as shown in figure 21. In summary, the resistive-type or diode-type thermometer are easily fabricated using standard CMOS process, and hence can be further integrated with the CMOS-MEMS humidity sensor to achieve a compact module for relative humidity sensing.

4.2. Other sensing types

Apart from the aforementioned capacitive humidity sensors, several other sensing mechanisms have been utilized to design humidity sensors and have been further implemented using the CMOS platform. More specifically, the resistivity and piezoresistivity of the poly-Si film inherent in the CMOS-platform have also been utilized to develop humidity sensors of other sensing types. For instance, as shown in figure 22(a), nanowire WO_3 prepared by sol-gel method, was adopted as the humidity sensing material, and this water vapor sensitive material was coated inside a micro-machined cavity (on top of the oxidized poly-Si layer) after the post-CMOS process [113]. To detect the humidity level changes, the poly-Si (on a CMOS chip prepared by the *TSMC* 2P4M processes), which acts as the sensing resistor, undergoes resistance changes when the sensing film adsorbs or desorbs water vapor. Moreover, the resonant type CMOS-MEMS humidity sensor were demonstrated in [126, 127]. As displayed in figure 22(b), the polysilicon electro-thermal actuated cantilevers, are fabricated on a chip prepared using the *ams* standard CMOS process, and then coated with polyimide [126]. The CMOS-MEMS cantilever acts as a resonator for humidity sensing. As water vapor is absorbed by the polyimide, the mass of the resonator will change, which further leads to a change in resonating frequency that can be detected by the poly-Si piezo-resistor. In short, the humidity sensing is achieved by measuring the resonant frequency change of the cantilever. A similar concept was also demonstrated in [127] by coating MgF_2 , a hygroscopic porous water vapor sensitive material, on a cantilever structure fabricated during the post-CMOS process. The poly-Si resistors are also used to detect the deflection of the cantilever structure. When the mass of sensing film changes due to humidity level variations, the resonant frequency of the oscillating micro cantilever also changes.

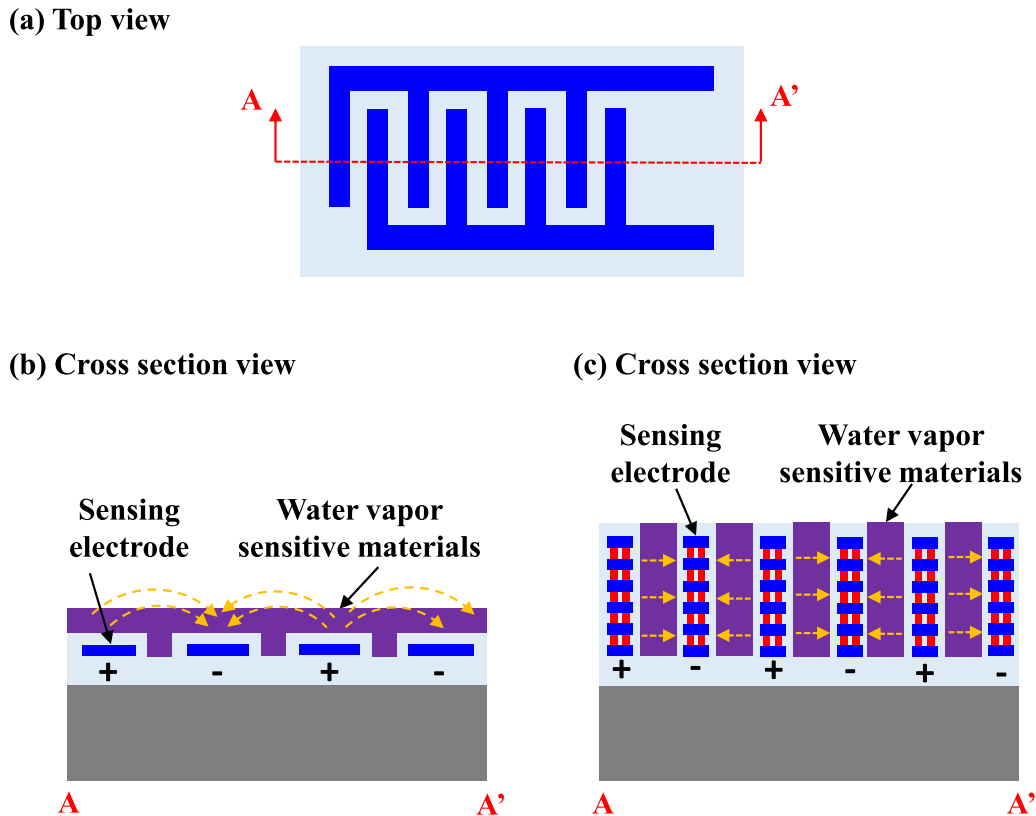


Figure 19. The schematic illustrations of the interdigitated electrode (IDE) structure design for the capacitive CMOS-MEMS humidity sensor: (a) top view and (b)–(c) cross section view.

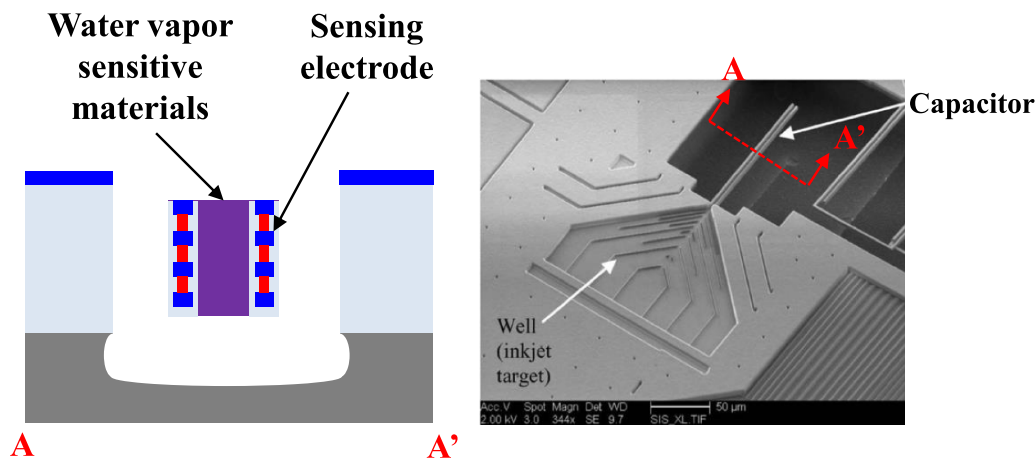


Figure 20. The schematic illustration and SEM micrograph of the CMOS-MEMS capacitive humidity sensors using dielectric layer etching, DRIE and isotropic etching to release the electrodes [121]. © [2009] IEEE. Reprinted, with permission, from [121].

4.3. Summary

This section reviewed CMOS-MEMS humidity sensors fabricated using various CMOS and post-CMOS processes, as summarized in table 3. The review indicates that the most common sensing mechanism for CMOS-MEMS humidity sensors is the capacitive type [116–124], and the response time and sensitivity are two typical indexes for performances. In this regard, the sensing materials and sensing electrodes are two major design concerns to enhance the performances of capacitive type humidity sensors. The CMOS compatible

polyimide is the primary water vapor sensing material for CMOS-MEMS capacitive humidity sensors [88, 116, 117, 120–123]. Other materials such as RF-aerogel [118, 119] and polypyrrole [124] have been studied to improve the response time. In addition, based on the available CMOS platform and the development of the post-CMOS processes, different sensing electrode designs (including the VPP [116–119], and IDE [121–123]) are demonstrated to enhance the response time and sensitivity. Moreover, the CMOS process containing the poly-Si layer as the piezo-resistive material together with the

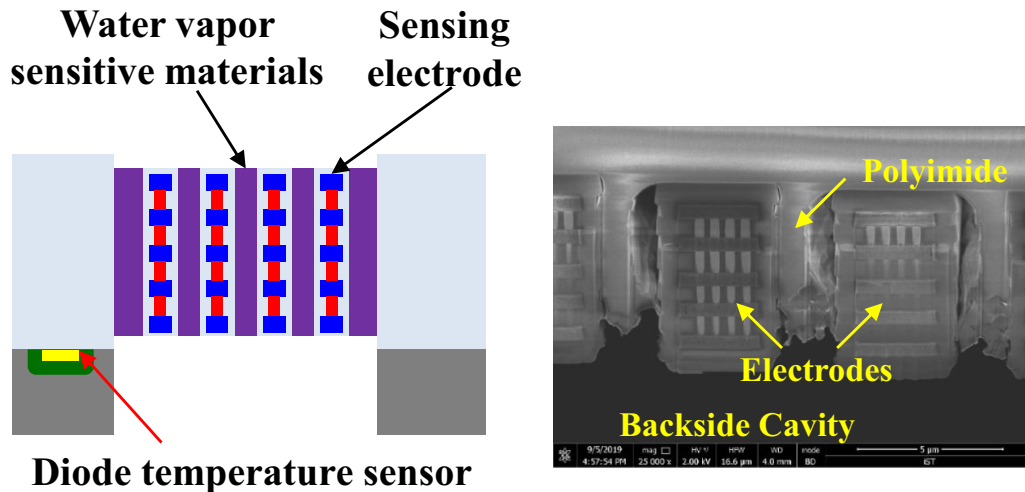


Figure 21. The schematic illustration and SEM micrograph of the CMOS-MEMS capacitive humidity sensors using double side post-CMOS etching processes [122]. © [2020] IEEE. Reprinted, with permission, from [122].

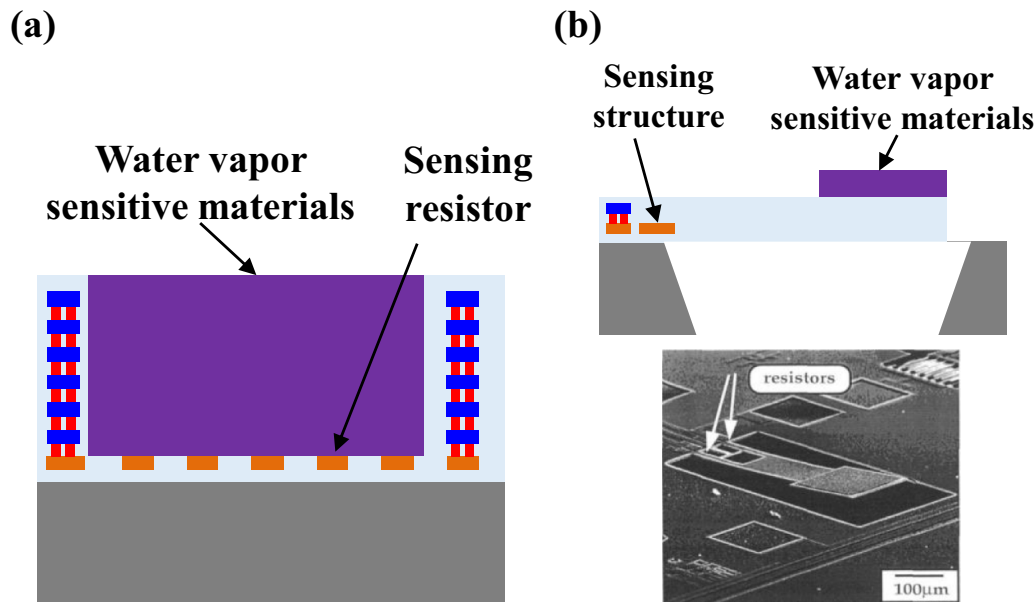


Figure 22. The schematic illustration and SEM micrograph of the other sensing types of humidity sensors: (a) resistivity [113] and (b) resonant type [126]. (b) Reproduced from [126]. © IOP Publishing Ltd All rights reserved.

post-CMOS micromachining technologies could be used to fabricate deformable and movable mechanical structures. As a result, CMOS-MEMS humidity sensors with the resistive type [113] and resonant type [126, 127] sensing mechanisms have also been investigated. Since the information of ambient temperature is required to determine the relative humidity, the CMOS-MEMS technology further showed its advantage of monolithically integrating the thermometer and humidity sensor on a single chip [88, 117, 122].

5. Gas sensors

The semiconductor and MEMS technologies could enable the size and cost reduction for gas sensors and further enlarge

their applications. Many different sensing mechanisms, such as the chemo-resistive [131, 132], electrochemical [133, 134], FET (field effect transistor) [135, 136], optical [137, 138], calorimetric [139], capacitance-based [140, 141], resonant [142], SAW (surface acoustic wave) [143], GC (gas chromatography) [144], holographic [145] and so on, have been exploited to develop miniaturized micromachined gas sensors. Presently many commercial gas sensors have been demonstrated using the MEMS technologies [146, 147]. By leveraging the post-CMOS micromachining processes [90, 130] and further depositing sensing materials, various gas sensors with monolithically integrated sensing circuits have also been realized using the CMOS platform. For example, as shown in figure 23(a), the CMOS-MEMS GC SoC in [144] consists of the chemo-resistive gas sensing unit and various signal

Table 3. CMOS-based humidity sensors with different sensing technique and their benefits/concerns.

Sensing type	Design/process features	Concerns	Sensing material	Platform	Response time	Sensitivity	Reference
Capacitive	<ul style="list-style-type: none"> • Low power consumption • Small (sub-micron) sensing gap between electrodes 	VPP electrodes	Polyimide	Other	4 s	0.21%/RH	[116]
	<ul style="list-style-type: none"> • Suspended thin film structures (residual stress of CMOS films) • Aspect ratio of sensing gap 	RF-aerogel	TSMC 0.18 μm process	16 s (τ ₉₀) 19 s (τ ₉₀) 6 s (τ ₉₀)	0.051%/RH 0.571%/RH 3.8 kHz/RH	[117] [118] [119]	
Resistive	<ul style="list-style-type: none"> • Large water vapor diffusion area 	IDE electrodes	Polyimide	TSMC 0.18 μm process	12.1 s (τ ₉₀)	2.90 fF/RH	[88]
	<ul style="list-style-type: none"> • Thermal influences (material, etc) • Relatively high power consumption 	Water vapor diffusion surface area	TSMC 0.35 μm process	3.1 s (τ ₆₃) N/A	4.06 fF/RH 14.5 kHz/RH	[122] [120]	
Resonant	<ul style="list-style-type: none"> • Fast response time 		Polyimide	Jazz Semiconductor	N/A	0.16–0.18%/RH	[121]
	<ul style="list-style-type: none"> • Relatively high power consumption 		Polyimide	0.35 μm process	<30 s (τ ₉₀)	0.9%/RH	[123]
Resistive	<ul style="list-style-type: none"> • Large water vapor diffusion area • Fast response time 		Polyimide	Faselec SACMOS	N/A	0.105 MHz/RH	[124]
	<ul style="list-style-type: none"> • Thermal influences (material, etc) • Relatively high power consumption 		Polyimide	TSMC 0.35 μm process	N/A	4.5 mV/RH	[113]
Resonant	<ul style="list-style-type: none"> • Fast response time 		Polyimide	TSMC 0.35 μm process	<30 s	270 Hz/RH	[126]
	<ul style="list-style-type: none"> • Relatively high power consumption 		MgF ₂	Mitel Corporation's 1.5 μm process	N/A	1.18 Hz/RH	[127]

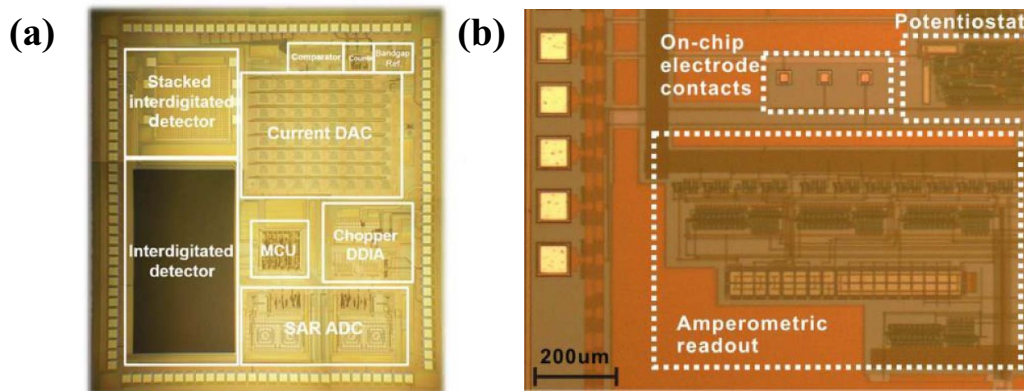


Figure 23. The schematic illustration of (a) μ GC chip and [144] (b) electrochemical sensor chip [148]. (a) © [2016] IEEE. Reprinted, with permission, from [144]. (b) © [2018] IEEE. Reprinted, with permission, from [148].

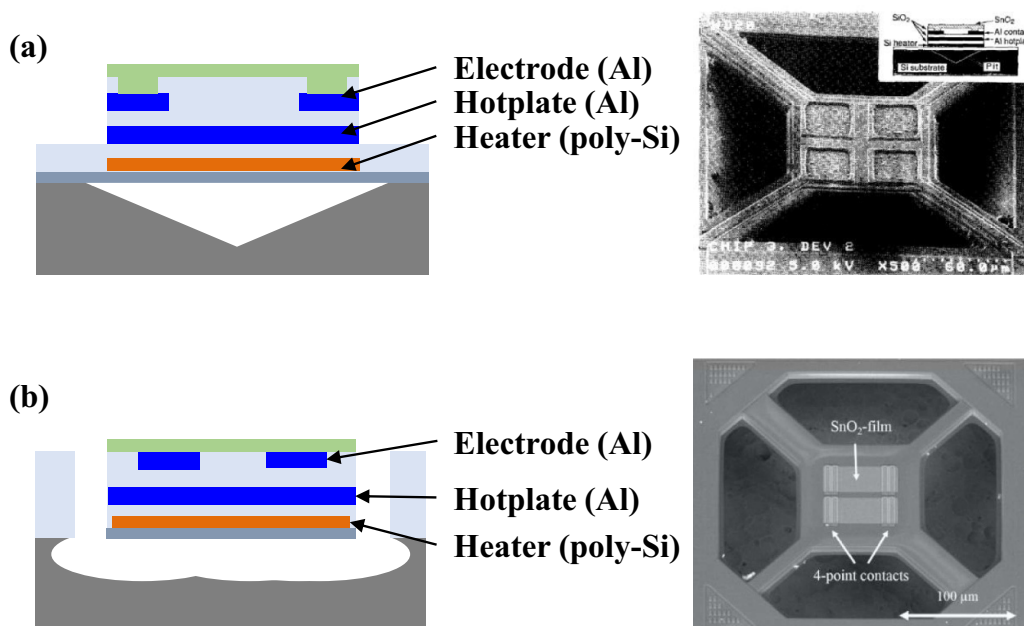


Figure 24. The schematic illustration and SEM micrograph of the typical chemo-resistive type gas sensor: (a) anisotropic Si etching by Ethylene diamine-pyrocatechol-water (EDP) [156] and (b) isotropic Si etching by XeF₂ [157, 158]. (a) © [1993] IEEE. Reprinted, with permission, from [156]. (b) Reproduced from [157]. CC BY NC-ND.

processing circuits such as the calibration circuit, analog to digital converter, the micro-control unit, and so on. Another example is the CMOS-MEMS gas sensor with potentiostat and amperometric readout, as displayed in figure 23(b) [148]. The gas sensors with the characteristics of multi-sensing and small size have also been commercialized by the CMOS-MEMS platform [149]. Moreover, the inherent materials for CMOS processes can be exploited to fabricate the necessary components of the gas sensor (such as the heater, thermometer, thermos-isolation structure, etc.), and the CMOS platforms can also provide the capability of integrating gas sensors with readout circuits to form monolithic sensing systems. Thus, the CMOS-MEMS technology is a promising approach for realizing environmental gas sensors. This section of the review will firstly exhibit the most common CMOS-MEMS gas sensors (the chemo-resistive type), and then followed by a brief discussion for other types of CMOS-MEMS gas sensors.

5.1. Chemo-resistive type gas sensor

The typical chemo-resistive type gas sensor, as shown in figure 24(a), consists of the following main components: gas sensing film, heater/hotplate, and electrode. The CMOS platforms offer available materials to fabricate the heater/hotplate and electrodes, yet the additional material (typically the metal-oxide semiconductor materials) is required to serve as the gas sensing film. The post-CMOS micromachining processes are used to define the shape of the structures (with embedded electrodes) to accommodate the gas sensing films and also to fabricate the cavity on the Si substrate for thermal-isolation. In addition, the metal-oxide sensing film is also deposited by the post-CMOS processes. The electrical resistivity of metal-oxide semiconductor sensing films will change when adsorbing (or desorbing) gas molecules, so the gas concentration can be detected through the variation of resistance [150–153]. The

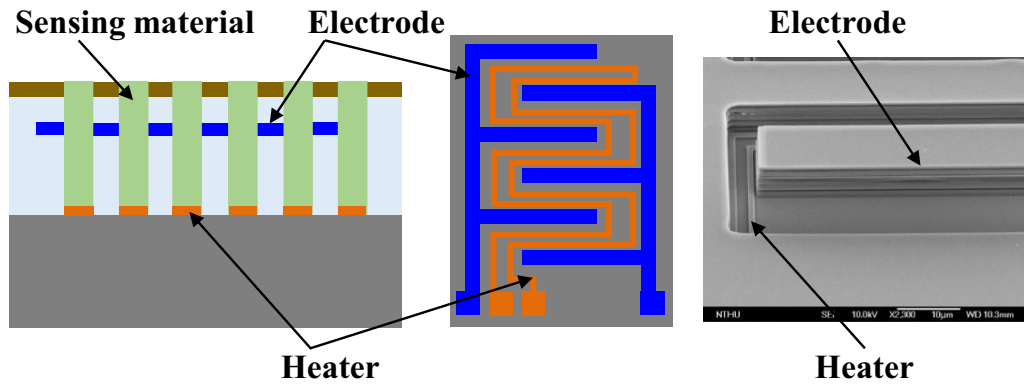


Figure 25. The schematic illustration and SEM micrograph of the chemo-resistive type gas sensor by novel heater design [159]. © [2019] IEEE. Reprinted, with permission, from [159].

heater/hotplate is used to define the operating temperature and to enable the temperature to be evenly distributed to increase the sensor's selectivity of target gas [154, 155], and the electrodes are utilized to readout the resistance change. Thus, the performance of gas sensors highly depends on the structure design for thermal management and the sensing film.

The structure design for chemo-resistive gas sensors is relatively simple, which may include the design of heater and hotplate for heating, and the design of Si cavity for thermal isolation. The poly-Si with its higher melting point is exploited to fabricate the heater, and the CMOS BEOL layers (metal and dielectric films) are used to define the electrodes and other required components. The metal layer with its higher thermal conductivity has also been used to fabricate the hotplate to improve the temperature uniformity during heating. In addition, to enhance the temperature control and the power consumption, the thermal isolation of sensor is a critical concern for structure design. Such gas sensing architectures are demonstrated in various designs. As shown in figure 24(a), the CMOS-MEMS gas sensor is fabricated on a CMOS chip prepared through the *MOSIS* foundry service [156]. The post-CMOS anisotropic bulk Si etching is used to release the sensor from the substrate for thermal isolation. Moreover, the sensing elements, including the heater, hotplate, electrodes, and sensing materials are supported by four beams to further reduce the thermal loss through the anchors. The heater is realized by using the oxide encapsulated poly-Si. The aluminum layers partitioned by the dielectric films are respectively used as the hotplate, the temperature sensor (TCR-based), and the electrodes/electrical routings. Thus, the sensor operating temperature as defined by the heater can be monitored by the TCR-based sensor. These layers (poly-Si, aluminum, dielectric layers) are all inherent materials in this CMOS process. However, the gas sensing materials are typically not available in the standard CMOS platforms. In this case, an additional thin film deposition is required in the post-CMOS process to prepare the SnO₂ gas sensing layer. More details about the deposition processes for sensing materials will be discussed later. In terms of thermal isolation, the post-CMOS isotropic Si etching process (by XeF₂) is employed in [157, 158] to release the sensor from the substrate, as shown in figure 24(b). The CMOS chip is fabricated by the *ams* 0.35 µm

standard CMOS process. Note that the sensor consists of multiple layers with different coefficient of thermal expansion (CTE), hence the thermal deformation of suspended structure under high temperature operation is a design concern. Moreover, the temperature elevation may cause the resistance change of metal electrodes to influence measurement results.

To properly manage the thermal influences, the heater is an important design consideration. Figure 25 displays a gas sensor integrated with a heater of novel design [159]. The CMOS chip is fabricated by the *TSMC* 0.35 µm 2P4M standard CMOS process. As compared with [160], this design has no contact between the heater and the interdigitated electrodes so as to avoid thermal influences during sensing. Moreover, this design also shortens the length of heater to reduce the resistance and power consumption. Note that the power consumption can be further reduced by suspending the sensor through bulk Si etching. In addition to poly-Si, the tungsten metal layers (acting as interconnect of circuits in CMOS BEOL) with high melting point have also been employed in [161] to fabricate the heater and hotplate of CMOS-MEMS gas sensor, as shown in figure 26(a). This gas sensor is fabricated by the *X-FAB* SOI-CMOS processes together with a post-CMOS backside DRIE Si etching for thermal isolation. The insulator of the SOI wafer serves as the etching stop layer for DRIE. Note that to pattern the tungsten layer for heater or hotplate may violate the design rules for some CMOS platforms. Figure 26(b) shows another novel heater design realized using the MOSFET array rather than the patterned poly-Si layer [162]. The MOSFET heater could reach a high temperature of 550 °C with a low power consumption of 16 mW and a fast thermal time constant of <10 ms. This gas sensor is also fabricated by the *X-FAB* SOI-CMOS processes and the post-CMOS backside Si etching. Thus, the MOSFET heater is implemented using the device Si layer of SOI. Note that by employing the tungsten and Si layers to form the heater [161, 162], the thermal drift caused by high temperature heating could be suppressed.

The selection of the sensing material for CMOS-MEMS gas sensors is another critical design concern. Major considerations for material selection are the thermal and deposition issues of the sensing film. Most of the gas sensing films are

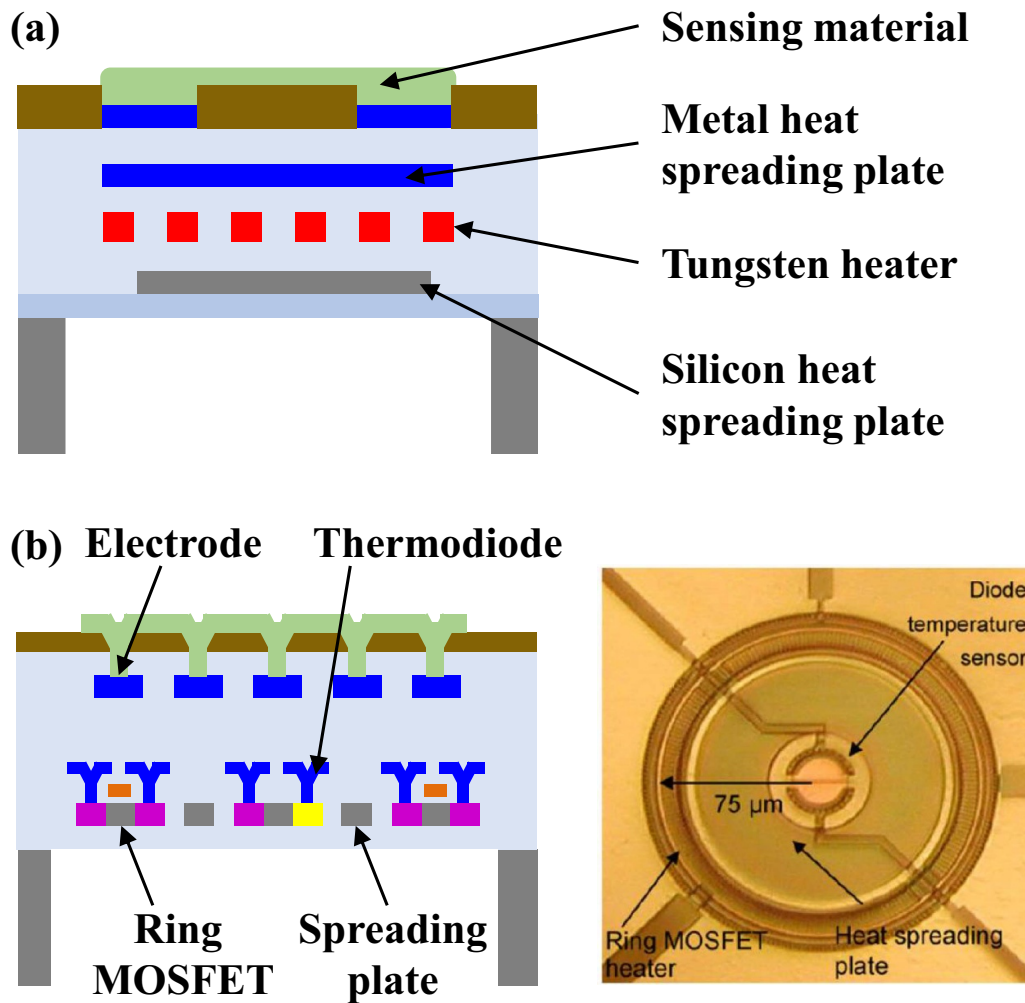


Figure 26. The schematic illustrations of the CMOS-MEMS chemo-resistive type gas sensors based on different heating materials: (a) tungsten heater and (b) ring MOSFET [162]. (b) Reprinted from [162], Copyright (2007), with permission from Elsevier.

not the inherent materials in the CMOS platform. These sensing materials typically need high annealing and operating temperatures. Since the chips fabricated by the CMOS platforms cannot sustain long-time high-temperature heating due to the thermal budget of the metal layers, it is important to select appropriate sensing materials that are CMOS-compatible. Presently, many metal-oxide semiconductor materials have been developed for gas sensors [163], such as SnO₂ [164], ZnO [165], TiO₂ [166], WO₃ [167], In₂O₃ [168], etc, and the annealing and operating temperature of these materials vary, falling between 250°C and 550°C [169]. Therefore, some commonly used sensing materials, such as WO₃, are not acceptable for use in CMOS-MEMS gas sensors due to their high annealing/operating temperatures. Among the aforementioned sensing films, the SnO₂ fulfills the thermal budget limit of the CMOS platform, and is therefore commonly used as the material for CMOS-MEMS gas sensors. Thus, this review will introduce various technologies, including the sputtering, spray pyrolysis, or drop casting, to deposit the SnO₂ as the sensing material for CMOS-MEMS gas sensors. The sputter deposition approach is employed in [156] to prepare the SnO₂ sensing material on the CMOS-MEMS chip, as

depicted in figure 24(a). This study also indicates that the grain sizes as well as the film properties of SnO₂ are influenced by the processing temperature, so that the heater on this sensor can be applied to modify the deposited film. Moreover, the spray pyrolysis technology was used to deposit the SnO₂ on the CMOS-MEMS chip [170]. As shown in figure 27(a), this deposition method could achieve a good coverage on the CMOS-MEMS chip with a step height of ~3 μm. The photolithography and Ar ion etching processes have been employed to pattern the SnO₂ sensing film after the post-CMOS spray pyrolysis deposition [156, 158]. Finally, the drop casting method is considered as a solution to deposit the sensing film when the process temperature exceeds the acceptable thermal budget of the CMOS chip. For example, as reported in [159, 160], the sensing material (SnO₂-ZnO) was synthesized using hydrothermal synthesis method with a maximum process temperature of 700 °C which exceeds the thermal budget of CMOS chip. By adopting drop casting, the sensing material can be easily deposited on the CMOS-MEMS chip, as shown in figure 27(b). However, it should be noted that the drop casting process cannot achieve batch fabrication and the patterning of the sensing material.

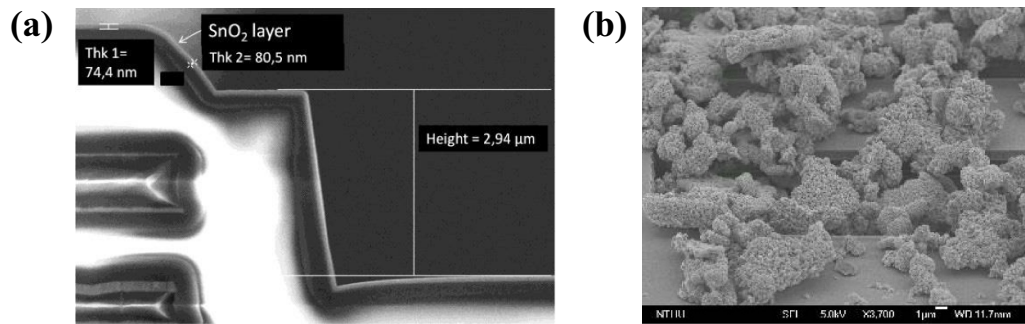


Figure 27. The SEM micrograph of different deposition method: (a) spray pyrolysis [170] and (b) drop casting [159]. (a) Reproduced from [170], CC BY NC-ND, and (b) Reproduced from [160]. CC BY.

5.2. Other sensing types

Apart from the aforementioned chemo-resistive approach, different sensing mechanisms to realize the CMOS-MEMS gas sensors have also been demonstrated. As reported in [148], the post-CMOS processes is illustrated in figure 28(a), which includes the deposition/patterning of Au/Ti electrode layers on a CMOS chip with sensing circuits, and then the casting of room-temperature-ion-liquid (RTIL) to realize the electrochemical type oxygen gas sensor. Due to the elimination of wiring parasitic and environmental noise, such CMOS-MEMS oxygen sensor with monolithically integrated sensing circuits shows an improvement in both response time and limit of detection. Moreover, as reported in [171, 172], the ZnO nanorod layer fabricated by the post-CMOS process was used as the sensing material to achieve FET type gas sensors. As shown in figure 28(b), the ZnO nanorods layer was deposited using the hydrothermal method to connect the interdigitated electrodes (including the control and the floating electrodes) on the CMOS chip. Based on the IR or the fluorescence quenching detections, the optical type CMOS-MEMS gas sensors have also been demonstrated in [173–175]. As reported in [173], the IR emitted from a light source can be absorbed by the target gas, and hence the gas concentration can be detected by the decayed intensity of IR. In addition to the IR emitter, the CMOS-MEMS thermopile reported in [176] is employed to act as the IR detector. The other optical type gas sensor is based on fluorescence quenching [174, 175], as displayed in figure 28(c). When the light emitted from the light source excites the sensing material, fluorescence will be produced. The target gas acts as the quencher to inhibit the intensity of fluorescence, and hence the gas concentration can be detected by measuring the fluorescence intensity. In [174, 175] the post-CMOS etching on a CMOS chip (standard TSMC 0.35 μm 2P4M process) was used to fabricate the optical gas sensor. The volume of the optical gas sensor can be reduced by the heterogeneous integration of the light emitting LED with the CMOS-MEMS chip.

5.3. Summary

This section shows CMOS-MEMS gas sensors fabricated using various CMOS and post-CMOS processes, as indicated in table 4. In addition to the most common chemo-resistive

type gas sensors, several counterparts of different sensing mechanisms (including the electrochemical, FET, and optical) have also been discussed. Typically, the performances, such as the sensitivity and power consumption of chemo-resistive type gas sensors, are highly dependent on the sensing materials and heater designs. The inherent materials in CMOS processes offer the necessary films to fabricate the heater, hot-plate, and electrodes of the chemo-resistive type gas sensors, and the MEMS bulk Si etching processes could realize the thermal-isolation cavity to further enhance sensor performances. Similar to the humidity sensors, the suspended structures of the gas sensors are fully or mostly anchored to the Si substrate. The un-wanted deformation by the residual stresses of CMOS BEOL films [129] and the CTE mismatch of the metal and dielectric films [129] have minor influences on the performances of CMOS-MEMS gas sensors. However, due to the frequent operating at low-high temperatures, the reliability of the structures consisted of multiple layer composite films could be a concern. The SnO_2 is one of the popular metal-oxide semiconductor sensing materials for chemo-resistive type gas sensor, and thermal budget is a critical concern for the post-CMOS deposition of sensing films. In addition, it is not straightforward to deposit the sensing materials using the batch fabrication process. On the other hand, no suspended thermal-isolation structures are required for the electrochemical, FET, and optical CMOS-MEMS gas sensors, these sensors have minor impact by the CTE mismatch and residual stresses of thin films [129].

6. Environment sensing hub

The integration of multiple sensors to form a sensing unit could offer more robust and comprehensive information for users. For instance, the inertial module consisted of the accelerometer, gyroscope and magnetometer has been demonstrated by the industry [177]. Through the fusion of different sensing signals received from these sensors, more accurate motion sensing can be achieved to fulfill requirements of indoor navigation, gesture recognition, etc. Note that the sensors in [177] are integrated by using packaging to offer a compact sensing module. Similarly, for environmental monitoring, useful information can also be achieved by fusing the sensing signals received from different environment

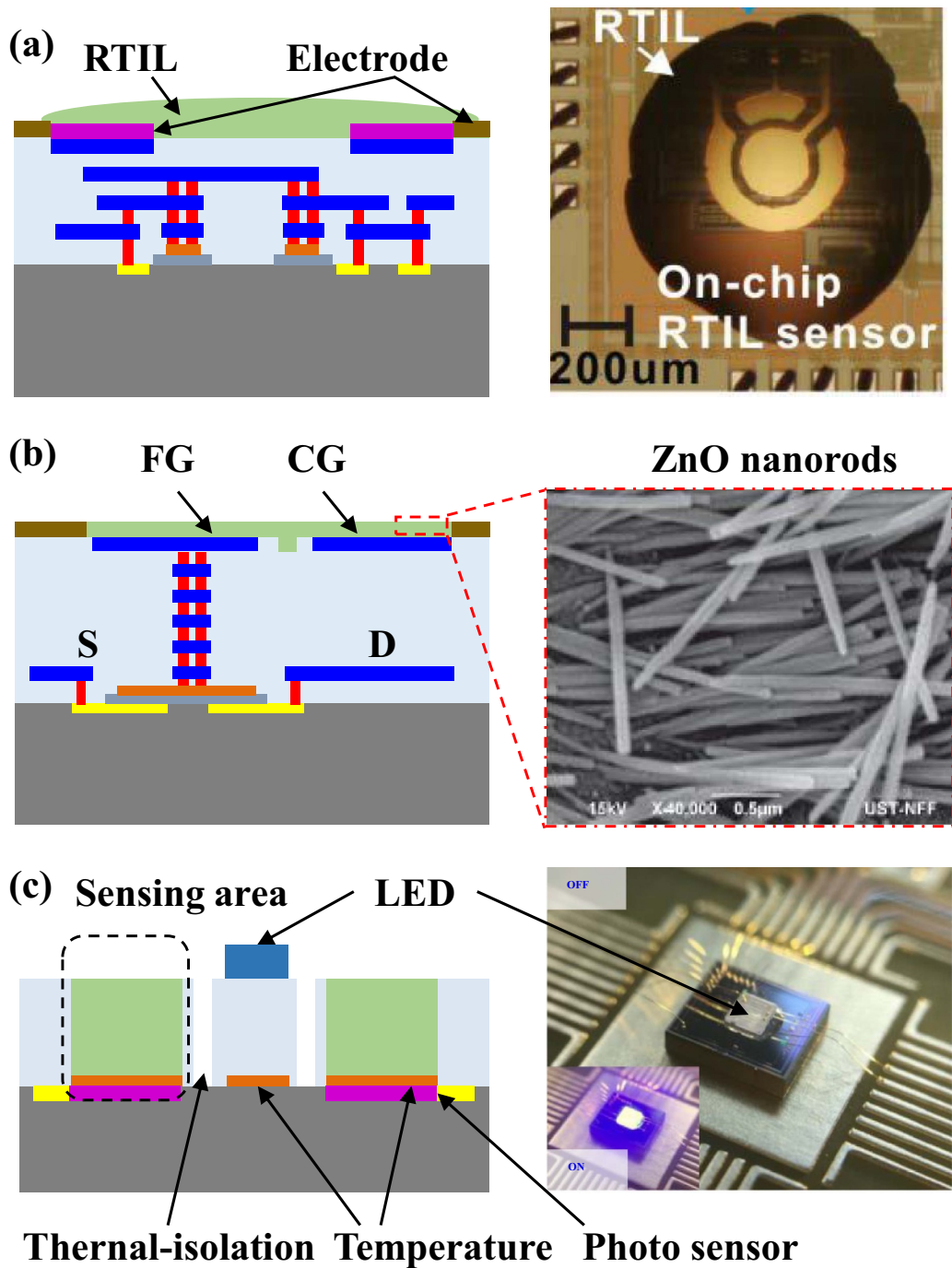


Figure 28. The schematic illustration and SEM micrograph of the other sensing types of gas sensors: (a) electrochemical type [148]. (b) FET type [171, 172] and optical type [175]. (a) © [2018] IEEE. Reprinted, with permission, from [148]; (b) © [2018] IEEE. Reprinted, with permission, from [171]; (c) © [2019] IEEE. Reprinted, with permission, from [175].

sensors. Moreover, the integration of sensing information is required for some applications, for example, as mentioned in section 4, the temperature measurement is needed for the humidity sensor to determine the relative humidity [117]. One of the advantages of CMOS-MEMS technology is to enable the monolithic integration of various sensors and their sensing circuits on a single chip to realize an even more compact sensing module. In this section, a few examples will be introduced

to show the possibility of sensor integration to form the environment sensing hub.

As reported in [122], the standard TSMC 0.18 μm 1P6M CMOS platform together with the double-side post-CMOS micromachining processes have been developed to implement the environment sensing hub. Figure 29(a) displays the environment sensing hub consisted of the humidity, pressure, and temperature sensors. The backside silicon etching could

Table 4. CMOS-based gas sensors with different sensing technique and their benefits/concerns.

Sensing type	Design/process features	Concerns	Platform	Sensing material	Target gas	Sensitivity	Reference
Chemo-resistive	<ul style="list-style-type: none"> • Heater material: polysilicon • Suspended structure (Microbridge) • Etching stop by crystal plane (EDP) • Sputter deposition 	<ul style="list-style-type: none"> • Residual stress issues • High temperature operation • Low selectivity 	MOSIS	SnO ₂	H ₂ /O ₂	N/A	[156]
	<ul style="list-style-type: none"> • Heater material: Polysilicon • Suspended structure (Microbridge) • Spray pyrolysis process • Heater material: Polysilicon • Drop casting 	<ul style="list-style-type: none"> • Residual stress issues • Etching time control (XeF₂) • High temperature operation • Low selectivity • Etching time control (Silox) • High power consumption • High temperature operation 	ams AG 0.35 μm standard CMOS process	SnO ₂	CO	N/A	[157, 158]
	<ul style="list-style-type: none"> • Heater material: Tungsten • The highest operating temperature • Suspended structure (DRIE), Membrane 	<ul style="list-style-type: none"> • Low selectivity • High cost (SOI-CMOS) • DRC of tungsten 	TSMC 0.35 μm 2P4M standard CMOS process	ZnO-SnO ₂	O ₂	0.3%/%, 0.2%/%	[159] [160]
	<ul style="list-style-type: none"> • Suspended structure (DRIE), Membrane • Heater material: Silicon (MOSFET) • Suspended structure (DRIE), Membrane • Low power consumption (@550 °C, 16 mW) 	<ul style="list-style-type: none"> • High cost (SOI-CMOS) 	X-Fab SOI CMOS process	N/A	N/A	N/A	[161]
		<ul style="list-style-type: none"> • High cost (SOI-CMOS) 	X-Fab 1.0 μm SOI CMOS process	N/A	N/A	N/A	[162]

(Continued.)

Table 4. (Continued.)

Sensing type	Design/process features	Concerns	Platform	Sensing material	Target gas	Sensitivity	Reference
	<ul style="list-style-type: none"> • Spray pyrolysis 	<ul style="list-style-type: none"> • Requires high temperature operation • Low selectivity • Additional lithography during post processes • Electrodes are easily contaminated/eroded 	N/A	SnO ₂	H ₂	N/A	[170]
Electro chemical	<ul style="list-style-type: none"> • Drop casting • Room temperature operation 	<ul style="list-style-type: none"> • Too sensitive to temperature • Complicated circuits 	0.5 μm CMOS process	RTIL	O ₂	4.23 mV/%	[148]
FET	<ul style="list-style-type: none"> • Low power consumption • Room temperature operation 	<ul style="list-style-type: none"> • Bulky system set-up • Additional light source • High cost • Additional excitation light source • High cost 	GlobalFoundries 0.18 μm 1P6M CMOS process	ZnO	acetone	N/A	[171, 172]
Optical detection	<ul style="list-style-type: none"> • High sensitivity and selectivity • Rapid response • Room temperature operation • High selectivity • Rapid response • Drop casting • Room temperature operation 		N/A	N/A	CO ₂	N/A	[173]
			TSMC 0.35 μm 2P4M standard CMOS process	C ₃₀ H ₂₄ C ₁₂ N ₆ Ru·6H ₂ O	O ₂	9.2 μA/%	[175]

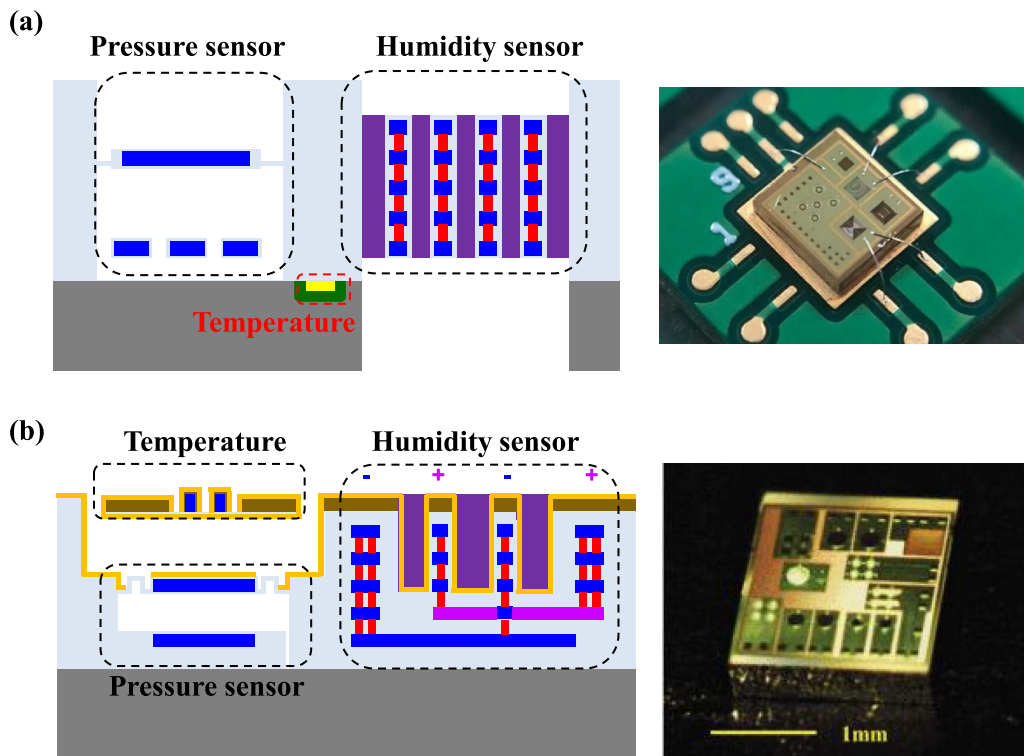


Figure 29. The schematic illustration and micrograph of the environment sensing hub: (a)–(b) the environment sensing hub consisted of the humidity, pressure, and temperature sensors [88, 122]. (a) © [2020] IEEE. Reprinted, with permission, from [88]. (b) © [2020] IEEE. Reprinted, with permission, from [122].

enable the diffusion of vapor from both sides of polyimide to reduce the response time of humidity sensor, as discussed in section 4 [122]. The backside silicon etching also creates the chamber volume for the pressure sensor, as mentioned in section 3 [122]. Moreover, the standard *TSMC* 0.18 μm 1P6M CMOS platform together with the single-side post-CMOS micromachining processes have been developed to implement the environment sensing hub illustrated in figure 29(b) [88]. Such an environment sensing hub is also composed of the humidity, pressure, and temperature sensors. The suspended flexible structures for pressure sensor and the sensing electrodes for the humidity sensor are defined by the front-side etching of sacrificial metal layers, as discussed in sections 2 and 4 [88]. The additional parylene sealing and polyimide dispensing are needed for pressure and humidity sensors, respectively. In short, these environment sensors are designed based on the same process scheme, so that they can be fabricated and monolithically integrated on the same chip. As compared with the system-in-packaging (SiP) approach in [177], a more compact environment sensing module is achieved using the SoC solution in [88, 122].

Another example is the gas sensor design based on the *TSMC* 0.35 μm 2P4M CMOS standard process along with the single-side post-CMOS micromachining processes [160, 175]. Figure 28(c) shows the environment sensing hub consisted of the vertically integrated gas and temperature sensors [160]. The monolithically integrated thermometer enables the on-site temperature monitoring and compensation. Similar as in for relative humidity detection, the temperature information is needed for the gas sensor to avoid

the drift of sensing signals [175]. In addition, the heater can also be fabricated and further integrated with the gas sensor by using the same process scheme, as displayed in figure 25 [159, 160]. In this environment sensing hub, the heater is exploited to heat the sensing material. The heating temperature of the heater can be specifically controlled, depending on the sensing film material and target sensing gas, to provide an enhancement in selectivity. The concept of a sensing hub has also been extended to integrate environment with inertial sensors for different applications. For example, the monolithic integration of temperature, linear acceleration, and pressure sensor has been demonstrated in [100, 178] to offer a compact tire pressure monitoring system (TPMS). The TPMS sensing module is implemented using the *TSMC* 0.35 μm 2P4M CMOS standard process together with the double-side post-CMOS micromachining processes. In summary, the CMOS-MEMS technologies could enable the monolithic integration of multiple sensors, actuators, and the related driving and sensing circuits to achieve a compact sensing hub for various applications.

7. Conclusions and future perspectives

In conclusion, the booming growth in environmental condition sensing and monitoring pushes the need of inexpensive environment sensors with small sizes and low power consumptions. The outbreak of COVID-19 further increases the need for fast monitoring of environment conditions. Thus, the MEMS technologies are considered as promising solutions to realize

the required environment sensors. The mature CMOS process platforms available in many foundries can be extended to fabricate MEMS sensors to offer the advantage of relatively easier commercialization. Moreover, by leveraging the characteristics of CMOS process platforms, the integration of multiple sensors and sensing circuits to form a compact sensing system can also be achieved. In sections 2–5, this paper respectively reviews five different environment sensors (including the IR, pressure (barometer), humidity/temperature, and gas sensors) using the CMOS-based MEMS technologies. The advantages and design concerns of sensors fabricated by different CMOS and post-CMOS processes are introduced and commented. In addition, section 6 further demonstrates the CMOS-MEMS environment sensing hub through the monolithic integration of multiple environment sensors.

The CMOS process platform with the advantages of small line width definition and multi-layers for electrical routings are especially promising to implement capacitive sensing devices such as the humidity and pressure sensors, and also provide an excellent opportunity to fabricate CMOS-MEMS IR sensors with large number of arrays, and also fulfill the circuit integration monolithically. Thus the size of pixels and their pitches can be reduced to improve the spatial resolution of MEMS IR sensor arrays [60, 64, 66] for the performance enhancement of thermal imagers. Furthermore, the increasing pixel number of thermal imagers adds up the complexity of electrical routing. CMOS platforms possess multiple metal layers and vias used in interconnection, proving high feasibility for electrical connection of large pixel number of thermal imagers [61, 179, 180]. Moreover, the suspended MEMS structures of environment sensors are mainly designed for thermal isolation (e.g. for the applications of IR and gas sensors) and vapor diffusion enhancement (e.g. for the applications of humidity sensors). Thus, except for pressure sensors, the deformation and motion of suspended structures are not the design concerns for most of the CMOS-MEMS environment sensors. These structures are fully (e.g. structures in figures 17–19, and 24) or largely (e.g. structures in figures 21, 23, and 25) anchored to the substrate. The major drawbacks of CMOS-MEMS structures such as the existing of un-wanted deformation by the thin film residual stresses [130] and the CTE mismatch of the metal and dielectric films [129] have minor influences on the performances of these environment sensors. Thus, the CMOS-MEMS humidity sensors have been successfully commercialized by Sensirion [181], and the commercial CMOS-MEMS IR sensors have been demonstrated by [20–23]. These products show the real applications and future perspective of the CMOS-MEMS technologies for the environment sensors. Nevertheless, the post-CMOS processes are still required to fabricate the environment sensors, and the issues regarding material and process compatibilities are critical concerns. For example, as compared with polyimide, some sensing materials such as RF-aerogel and polypyrrole could reduce the response time of humidity sensors, yet their availability for the existing mature processes remains the concern for commercialization [118, 119]. Similarly, as limited by the process compatibility, it is not straightforward to batch fabricate the outstanding functional material Au-black on the CMOS-MEMS IR sensors

[54]. In addition, heating process is required during the operation of the humidity and gas sensors.

Moreover, many commercial products show the importance or the need of devices integration. As shown in [181–184], these humidity sensors are equipped with heater to avoid the water vapor condensation under a high relative humidity environment. The gas sensor (IR detection) equipped with humidity and temperature sensors for environment compensation is exhibited in [188]. Thus, by leveraging the characteristics of CMOS processes, the CMOS-MEMS technologies could enable the monolithic integration of different sensors, actuators, and sensing circuits to fulfill diversified requirements for wide applications. For example, the monolithic integration of heater and gas sensor using the CMOS-MEMS technologies are demonstrated in [156–160]. The monolithic integration of humidity and temperature sensors are also achieved in [88, 89, 117]. Moreover, the CMOS-MEMS gas sensing chip by integrating gas sensors and signal processing circuits (e.g. the calibration circuit, analog to digital converter, the micro-control unit, and so on) is presented in [144]. The integration of the sensor array for gas sensing [156, 174] and IR thermal imager [46, 51, 53, 63, 64, 73, 78] have also been demonstrated by the CMOS-MEMS technologies. As a final example, the humidity, pressure, and temperature sensors are monolithically integrated in the CMOS-MEMS chip to realize a compact environment sensing hub [88, 89]. As a future perspective, the CMOS-MEMS technologies could enable the integration of various MEMS components and sensing circuits to offer different advantages for environment sensors, such as the device footprint reduction, sensing signal enhancement, power consumption reduction, and so on. It is also worth to note that the yield and cost issues cannot be ignored while using the advanced CMOS platforms for environment sensors integration. The vertical stacking of CMOS chip and MEMS components through the wafer-level bonding would be another option for CMOS-MEMS integration [185, 186].

Process development is a major bottleneck to commercialize MEMS products. Since the CMOS platforms are mature process schemes and can be offered by various commercial foundries, the CMOS-MEMS technology is a cost-effective solution to realize miniaturized environment sensors by using the existing fabrication resources. On the other hand, as the CMOS process scheme is approaching its physical limitation, the CMOS-MEMS technology could be adopted to extend the applications of semiconductor industries. Thus, other than the ‘miniaturization (More Moore)’, the ‘diversification (More than Moore)’ would be another focus for semiconductor industries [187].

Data availability statement

No new data were created or analyzed in this study.

Acknowledgments

This project was supported by the Ministry of Science and Technology (MOST) of Taiwan under the Grant Nos.

MOST 109-2218-E-007-015, MOST 109-2923-E-007-007 and MOST 109-2926-I-007-503. The authors wish to appreciate the Taiwan Semiconductor Research Institute (TSRI), and Hsinchu Science Park Bureau, Taiwan, for the supporting of the technical and financial support.

ORCID iD

Weileun Fang  <https://orcid.org/0000-0002-6000-026X>

References

- [1] Analog Devices Sensors and MEMS (available at: www.analog.com/en/index.html)
- [2] Honeywell Navigation & Sensors (available at: <https://aerospace.honeywell.com/en/learn/products/sensors>)
- [3] Texas Instruments DLP products (available at: www.ti.com/dlp-chip/overview.html)
- [4] Hewlett-Packard Scanjet (available at: <https://store.hp.com/us/en/mlp/scanjet>)
- [5] Robert Bosch Pressure sensors (available at: www.bosch-sensortec.com/products/environmental-sensors/pressure-sensors/)
- [6] STMicroelectronics Accelerometers (available at: www.st.com/en/mems-and-sensors/accelerometers.html#products)
- [7] TDK InvenSense 6 axis motion tracking (available at: <https://invensense.tdk.com/products/motion-tracking/6-axis/>)
- [8] Knowles Smart Microphones (available at: www.knowles.com/products/smart-mics)
- [9] Infineon MEMS Microphones (available at: www.infineon.com/cms/en/product/sensor/mems-microphones/)
- [10] Robert Bosch Accelerometers (available at: www.bosch-sensortec.com/products/motion-sensors/accelerometers/)
- [11] Sensirion Humidity Sensors (available at: www.sensirion.com/en/environmental-sensors/humidity-sensors/)
- [12] Polar Optical-heart-rate-sensor (available at: www.polar.com/us-en/products/accessories/oh1-optical-heart-rate-sensor)
- [13] ROHM Optical Sensor for Heart Rate Monitor (available at: www.rohm.com/products/sensors-mems/optical-sensor-for-heart-rate-monitor/bh1790glc-product)
- [14] STMicroelectronics Humidity Sensors (available at: www.st.com/en/mems-and-sensors/humidity-sensors.html)
- [15] Robert Bosch Humidity sensors (available at: www.bosch-sensortec.com/products/environmental-sensors/humidity-sensors-bme280/)
- [16] Infineon Pressure Sensors (available at: www.infineon.com/cms/en/product/sensor/pressure-sensors/)
- [17] All Sensors Barometric Special (available at: www.allsensors.com/products/barometric-special)
- [18] Amphenol Pressure Sensors (available at: www.amphenol-sensors.com/en/mems-pressure-sensors)
- [19] STMicroelectronics Temperature Sensors (available at: www.st.com/en/mems-and-sensors/temperature-sensors.html)
- [20] Omron Sensors (available at: <https://components.omron.com/parametric-search?nodeId=404010&nodeParentId=4040>)
- [21] Heimann Products (available at: www.heimannsensor.com/)
- [22] Teledyne DALSA Infrared Detectors (available at: www.teledynedalsa.com/en/products/imaging/infrared-detectors/)
- [23] Pixart Far Infrared Sensor (available at: www.pixart.com/products-comparison/tw/33/)
- [24] Figaro Products (available at: www.figarosensor.com/product/feature/tgs8100.html)
- [25] Infineon CO2 Sensors (available at: www.infineon.com/cms/en/product/sensor/co2-sensors/?gclid=Cj0KCQiAjKqABhDLARIsABbJrGmFrqpfPLcOAKb5iLqQ1wPkEaID-lzb8nsJetdUTgHM9v0qOHLr0kcaAqUPEALw_wcB&gclsrc=aw.ds)
- [26] I-Blades Portable air quality monitor technology (available at: <https://i-blades.com/pages/portable-air-quality-monitor-technology>)
- [27] Bustillo J M, Howe R T and Muller R S 1998 Surface micromachining for microelectromechanical systems *Proc. IEEE* **86** 1552–74
- [28] Kovacs G T A, Maluf N I and Petersen K E 1998 Bulk micromachining of silicon *Proc. IEEE* **86** 1536–51
- [29] Lu Y and Horsley D A 2015 Modeling, fabrication, and characterization of piezoelectric micromachined ultrasonic transducer arrays based on cavity SOI wafers *J. Micromech. Microeng.* **24** 1142–9 (<https://ieeexplore.ieee.org/document/7014229>)
- [30] Xie H and Fedder G K 2003 Fabrication, characterization, and analysis of a DRIE CMOS-MEMS gyroscope *IEEE Sens. J.* **3** 622–31
- [31] Liu Y, Sun C, Lin L, Tsai M and Fang W 2009 A tunable range/sensitivity CMOS-MEMS capacitive tactile sensor with polymer fill-in technique *TRANSDUCERS 2009-2009 Int. Solid-State Sensors, Actuators and Microsystems Conf. (Denver, CO)* pp 2190–3 (<https://ieeexplore.ieee.org/document/5285611>)
- [32] Chang C, Tsai M, Sun C and Fang W 2014 Development of CMOS-MEMS in-plane magnetic coils for application as a three-axis resonant magnetic sensor *J. Micromech. Microeng.* **24** 035016
- [33] Sun C, Tsai M, Liu Y and Fang W 2010 Implementation of a monolithic single proof-mass tri-axis accelerometer using CMOS-MEMS technique *J. Micromech. Microeng.* **57** 1670–9 (<https://ieeexplore.ieee.org/document/5467179>)
- [34] Ho C-Y, Lee F-Y and Fang W 2017 Development of a CMOS-MEMS gyroscope using pure-oxide and symmetric metal-oxide stacking structures *IEEE transducers (Kaohsiung, Taiwan)* pp 1128–31 (<https://ieeexplore.ieee.org/document/7994251>)
- [35] Mao W-J, Cheng C-L, Lo S-C, Chen Y-S and Fang W 2017 Design and implementation of a CMOS-MEMS microphone without the back-plate *2017 19th Int. Conf. on Solid-State Sensors, Actuators and Microsystems IEEE Transducers (Kaohsiung, Taiwan)* pp 1037–40 (<https://ieeexplore.ieee.org/document/7994229>)
- [36] Lee J-H, Yeh S-K and Fang W 2020 Vertically integrated double-bridge design for CMOS-MEMS tri-axial piezo-resistive force sensor *IEEE MEMS (Vancouver, Canada)* pp 693–6 (<https://ieeexplore.ieee.org/document/9056191>)
- [37] Lopez J L, Verd J, Teva J, Murillo G, Giner J, Torres F, Uranga A, Abadal G and Barniol N 2009 Integration of RF-MEMS resonators on submicrometric commercial CMOS technologies *J. Micromech. Microeng.* **19** 015002
- [38] Kuo F-Y, Lin C-Y, Chuang P-C, Chien C-L, Yeh Y-L and Wen S K A 2017 Monolithic multi-sensor design with resonator-based MEMS structures *IEEE J. Electron Devices Soc.* **5** 214–8
- [39] Sheu M-L and Tsao L-J 2016 A sub-fF capacitive fingerprint sensor with neighbor pixel difference sensing *The 5th Int. Symp. on Next-Generation Electronics (Hsinchu, Taiwan)* pp 1–2 (<https://ieeexplore.ieee.org/document/7543362>)

- [40] Liu T-Y, Sung C-A, Weng C-H, Chu C-C, Zope A A, Pillai G and Li S-S 2018 Gated CMOS-MEMS thermal-piezoresistive oscillator-based PM2.5 sensor with enhanced particle collection efficiency *IEEE MEMS (Belfast, UK)* pp 75–8 (<https://ieeexplore.ieee.org/document/8346486>)
- [41] Sensirion Differential Pressure Sensors (available at: www.sensirion.com/en/flow-sensors/differential-pressure-sensor/)
- [42] Wei C, Lin Y, Hu Y, Wu C, Shih C, Huang C and Chang S 2006 Partial-electroded ZnO pyroelectric sensors for responsivity improvement *Sens. Actuators A* **128** 18–24
- [43] Akin T 2020 Low-Cost LWIR-Band CMOS Infrared (CIR) microbolometers for high volume applications *IEEE MEMS (Vancouver, Canada)* pp 147–52 (<https://ieeexplore.ieee.org/document/9056383>)
- [44] Shen T-W, Chang K-C, Sun C-M and Fang W 2019 Performance enhance of CMOS-MEMS thermoelectric infrared sensor by using sensing material and structure design *Micromech. Microeng.* **29** 025007
- [45] Shen T-W, Lee Y-C and Fang W 2018 Responsivity enhancement of CMOS-MEMS thermoelectric infrared sensor by heat transduction absorber design *IEEE MEMS (Belfast, UK)* pp 30–32 (<https://ieeexplore.ieee.org/document/8346473>)
- [46] Schaufelbuhl A et al 2011 Uncooled low-cost thermal imager based on micromachined CMOS integrated sensor array *J. Microelectromech. Syst.* **10** 503–10
- [47] Baltes H, Paul O and Brand O 1998 Micromachined thermally based CMOS microsensors *Proc. IEEE* **86** 1660–78
- [48] Budzier H and Gerlach G 2011 *Thermal Infrared Sensors: Theory, Optimisation and Practice* (New York: Wiley)
- [49] Lenggenhager R, Baltes H and Elbel T 1993 Thermoelectric infrared sensors in CMOS technology *Sens. Actuators A* **37–38** 216–20
- [50] Chang K-C, Lee Y-C, Sun C-M and Fang W 2017 Novel absorber membrane and thermocouple designs for CMOS-MEMS thermoelectric infrared sensor *IEEE MEMS (Las Vegas, NV, USA)* pp 1228–31 (<https://ieeexplore.ieee.org/document/7863638>)
- [51] Tanaka J, Shiozaki M, Aita F, Seki T and Oba M 2014 Thermopile infrared array sensor for human detector application *IEEE MEMS (San Francisco, CA, USA)* pp 1213–6 (<https://ieeexplore.ieee.org/document/6765866>)
- [52] Baer W G, Najafi K, Wise K D and Toth R S 1995 A 32-element micromachined thermal imager with on-chip multiplexing *Sens. Actuators A* **48** 47–54
- [53] Hirota M, Nakajima Y, Saito M and Uchiyama M 2007 120×90 element thermoelectric infrared focal plane array with precisely patterned Au-black absorber *Sens. Actuators A* **135** 146–51
- [54] Chen C 2011 Temperature error analysis and parameter extraction of an 8μm–14μm thermopile with a wavelength-independent absorber for tympanic thermometer *IEEE Sens. J.* **11** 2310–7 (<https://ieeexplore.ieee.org/document/5741821>)
- [55] Ogawaa S, Takagawab Y and Kimataba M 2018 Broadband polarization-selective uncooled infrared sensors using tapered plasmonic micrograting absorbers *Sens. Actuators A* **269** 563–8
- [56] Lin P-S, Shen T-W, Chan K-C and Fang W 2020 CMOS MEMS thermoelectric infrared sensor with plasmonic metamaterial absorber for selective wavelength absorption and responsivity enhancement *IEEE Sens. J.* **20** 11105–14
- [57] Lin P-S, Shen T-W, Chang K-C and Fang W 2020 Monolithic integration of plasmonic meta-material absorber with CMOS-MEMs infrared sensor for responsivity enhancement and human detection application *IEEE MEMS (Vancouver, Canada)* pp 157–60 (<https://ieeexplore.ieee.org/document/9056382>)
- [58] Schieferdecker J, Quad R, Holzenkämpfer E and Schulze M 1995 Infrared thermopile sensors with high sensitivity and very low temperature coefficient *Sens. Actuators A* **47** 422–7
- [59] Tezcan D, Eminoglu S and Akin T 2003 A low-cost uncooled infrared microbolometer detector in standard CMOS technology *IEEE Trans. Electron Devices* **50** 494–502
- [60] Mottin E, Bain A, Martin J, Ouvrier-Buffet J, Bisotto S, Yon J J and Tissot J L 2003 Uncooled amorphous silicon technology enhancement for 25 μm pixel pitch achievement *Proc. SPIE* **4820** 200–7 (<https://www.spiedigitallibrary.org/conference-proceedings-of-spie/4820/1/Uncooled-amorphous-silicon-technology-enhancement-for-25-um-pixel-pitch/10.1117/12.464848.full?SSO=1>)
- [61] Celik O et al 2020 640 x 480 17 um microbolometer uncooled detector development at ASELSAN, Inc. *Proc. SPIE* **11407** 1140719 (<https://www.spiedigitallibrary.org/conference-proceedings-of-spie/11407/2557669/640-x-480-17-um-microbolometer-uncooled-detector-development-at/10.1117/12.2557669.full>)
- [62] Abbasi S, Shafique A, Ceylan O, Kaynak C B, Kaynak M and Gurbuz Y 2018 A Test platform for the noise characterization of SiGe microbolometer ROICs *IEEE Sens. J.* **18** 6217–23
- [63] Leonov V, Perova N, Moor P D, Bois B D, Goessens C, Grietens B, Verbist A, Hoof C V and Vermeiren J 2003 Micromachined poly-SiGe bolometer arrays for infrared imaging and spectroscopy *Proc. SPIE* **4945** 54–63 (<https://www.spiedigitallibrary.org/conference-proceedings-of-spie/4945/1/Micromachined-poly-SiGe-bolometer-arrays-for-infrared-imaging-and-spectroscopy/10.1117/12.468410.full>)
- [64] Eminoglu S, Tanrikulu M and Akin T 2008 A low-cost 128×128 uncooled infrared detector array in CMOS process *J. Microelectromech. Syst.* **17** 20–30
- [65] Ishikawa T, Ueno M, Nakaki Y, Endo K, Ohta Y, Nakanishi J, Kosasayama Y, Yagi H, Sone T and Kimata M 2000 Performance of 320 x 240 uncooled IRFPA with SOI diode detectors *Proc. SPIE* **4130** 152–9 (<https://www.spiedigitallibrary.org/conference-proceedings-of-spie/4130/1/Performance-of-320-x-240-uncooled-IRFPA-with-SOI-diode/10.1117/12.409857.full>)
- [66] Kwon H et al 2011 A SOI-based CMOS-MEMS IR image sensor with partially released reference pixels *J. Micromech. Microeng.* **21** 025028
- [67] Rowe D M 1995 *CRC Handbook of Thermoelectrics* (Boca Raton, FL: CRC Press)
- [68] Hopper R, Ali S, Chowdhury M, Boual S, De Luca A, Gardner J W and Udrea F 2014 A CMOS-MEMS thermopile with an integrated temperature sensing diode for mid-IR thermometry *Procedia Eng.* **87** 1127–30
- [69] Xu D, Xiong B and Wang Y 2010 Design, fabrication and characterization of a front-etched micromachined thermopile for IR detection *J. Micromech. Microeng.* **20** 115004
- [70] Müller M, Budde W, Gottfried-Gottfried R, Hübel A, Jähne R and Kück H 1996 A thermoelectric infrared radiation sensor with monolithically integrated amplifier stage and temperature sensor *Sens. Actuators A* **54** 601–5
- [71] Van Herwaarden A W, Van Duyn D C, Van Oudheusden B W and Sarro P M 1989 Integrated thermopile sensors *Sens. Actuators* **22** 621–30
- [72] Cheng H, Huang Z, Lo S, Wang Y, Wu M and Fang W 2019 Piezoelectric MEMS microspeaker with suspension springs and dual electrode to enhance sound pressure level

- IEEE MEMS (Seoul, South Korea)* pp 767–70 (<https://ieeexplore.ieee.org/document/8870822>)
- [73] Chen S-J, Choe Y, Baumgartel L, Lin A and Kim E S 2012 Edge-released, piezoelectric MEMS acoustic transducers in array configuration *Micromech. Microeng.* **22** 025005
- [74] Xu D, Xiong B, Wang Y, Liu M and Li T 2009 Integrated micromachined thermopile IR detectors with an XeF₂ dry-etching process *J. Micromech. Microeng.* **19** 125003
- [75] Modarres-Zadeh M J and Abdolvand R 2014 High-responsivity thermoelectric infrared detectors with stand-alone sub-micrometer polysilicon wires *J. Micromech. Microeng.* **24** 125013
- [76] Roncaglia A, Mancarella F and Cardinali G 2007 CMOS-compatible fabrication of thermopiles with high sensitivity in the 3–5 μm atmospheric window *Sens. Actuators B* **125** 214–23
- [77] Akin T 2005 *CMOS-based Thermal Sensors* (Weinheim, DE: Wiley-VCH)
- [78] Niklaus F, Vieider C and Jakobsen H 2008 MEMS-based uncooled infrared bolometer arrays: a review *Proc. SPIE* **6836** 68360D (<https://www.spiedigitallibrary.org/conference-proceedings-of-spie/6836/1/MEMS-based-uncooled-infrared-bolometer-arrays-a-review/10.1117/12.755128.full>)
- [79] BOSCHE Pressure sensors (available at: www.bosch-sensortec.com/products/environmental-sensors/pressure-sensors/pressure-sensors-bmp390.html)
- [80] Infineon Pressure Sensors for IoT (available at: www.infineon.com/cms/en/product/sensor/pressure-sensors/pressure-sensors-for-iot/dps310/)
- [81] ST High-performance MEMS nano pressure sensor:260-1260 hPa absolute digital output barometer (available at: www.st.com/resource/en/datasheet/lps22hh.pdf)
- [82] Wilson J R, Vandyke J W and Rogers M S 2019 Electronic devices having electrically adjustable optical layers *United States Patent Application: 20190384062*
- [83] Omron Sensor Technology to Realize Continuous Blood Pressure Monitoring (available at: www.omron.com/global/en/technology/omrontechnics/vol50/004.html?fbclid=IwAR1svO_40fhoEuW43899vbMcHSfhNJZsr9DF5qy5L8plP0wWpaYENMvfyGY)
- [84] Sensirion Pulse Monitor with Differential Pressure Sensor (available at: <https://developer.sensirion.com/labs/pulse-monitor-with-differential-pressure-sensor/?fbclid=IwAR0tIzlwX9-WrMaUXfflBrO2sDwbA7j7gndhu6JKQwOGaKuN4VxckVUduE>)
- [85] TSMC MEMS Technology (available at: www.tsmc.com/english/dedicatedFoundry/technology/specialty/mems)
- [86] eeNEWS EUROPE Samsung leads the adoption of pressure sensors in Smartphones, for floor-accurate indoor geolocation (available at: www.eenewseurope.com/news/samsung-leads-adoption-pressure-sensors-smartphones-floor-accurate-indoor-geolocation/page/0/?fbclid=IwAR2uBwD242HDiBtu4g9l-oS2FFjCD4f_4hXoNctHbB9CAhQoUrM4sH9qJuE)
- [87] Lin W-C, Cheng C-L, Wu C-L and Fang W 2017 Sensitivity improvement for CMOS-MEMS capacitive pressure sensor using double deformable diaphragms with trenches *IEEE Transducers (Kaohsiung, Taiwan)* pp 782–5 (<https://ieeexplore.ieee.org/document/7994165>)
- [88] Lin Y-C, Hong P-H, Yeh S-K, Chang C-C and Fang W 2020 Monolithic integration of pressure/humidity/temperature sensors for CMOS-mems environmental sensing hub with structure designs for performances enhancement *IEEE MEMS (Vancouver, Canada)* pp 54–7 (<https://ieeexplore.ieee.org/document/9056401>)
- [89] Cheng C-L, Chang H-C, Chang C-I and Fang W 2015 Development of a CMOS MEMS pressure sensor with a mechanical force-displacement transduction structure *J. Micromech. Microeng.* **25** 125024
- [90] Fedder G K 2005 CMOS based sensors *IEEE Sensors Conf. (Irvine, CA, USA)* pp 125–8 (<https://ieeexplore.ieee.org/document/1597652>)
- [91] Dai C-L, Lu P-W, Chang C and Liu C-Y 2009 Capacitive micro pressure sensor integrated with a ring oscillator circuit on chip *Sensors* **9** 10158–70
- [92] Jang M and Yun K-S 2017 MEMS capacitive pressure sensor monolithically integrated with CMOS readout circuit by using post CMOS processes *Micro Nano Syst. Lett.* **5** 4
- [93] Deng F, He Y, Wu X and Fu Z 2014 A CMOS pressure sensor with integrated interface for passive RFID applications *Meas. Sci. Technol.* **25** 125104
- [94] Fujimori T, Hanaoka Y, Fujisaki K, Yokoyama N and Fukuda H 2005 Fully CMOS compatible on-LSI capacitive pressure sensor fabricated using standard back-end-of-line processes *IEEE Transducers (Seoul, South Korea)* pp 37–40 (<https://ieeexplore.ieee.org/document/1496353>)
- [95] Narducci M, Liu Y-C, Fang W and Tsai J 2013 CMOS MEMS capacitive absolute pressure sensor *J. Micromech. Microeng.* **23** 055007
- [96] Sundararajan A D and Hasan S R 2014 Post-processing and performance analysis of BEOL integrated MEMS pressure sensor capacitors in 8-metal 130 nm CMOS *Microelectron. Eng.* **119** 89–94
- [97] Ke F, Miao J and Wang Z 2009 A wafer-scale encapsulated RF MEMS switch with a stress-reduced corrugated diaphragm *Sens. Actuators A* **151** 237–43
- [98] Földner M, Dehé A and Lerch R 2005 Analytical analysis and finite element simulation of advanced membranes for silicon microphones *IEEE Sens. J.* **5** 857–63
- [99] Huang C-H, Lee C-H, Hsieh T-M, Tsao L-C, Wu S, Liou J-C, Wang M-Y, Chen L-C, Yip M-C and Fang W 2011 Implementation of the CMOS MEMS condenser microphone with corrugated metal diaphragm and silicon back-plate *Sensors* **11** 6257–69
- [100] Sun C-M, Wang C, Tsai M-H, Hsieh H-S and Fang W 2008 Monolithic integration of capacitive sensors using a double-side CMOS MEMS post process *J. Micromech. Microeng.* **19** 015023
- [101] Chavan A V and Wise K D 2002 A monolithic fully-integrated vacuum-sealed CMOS pressure sensor *IEEE Trans. Electron Devices* **49** 164–9
- [102] Kanda Y 1982 A Graphical Representation of the Piezoresistance Coefficients in Silicon *IEEE Trans. Electron Devices* **29** 64–70
- [103] Li X, Liu Q, Pang S, Xu K, Tang H and Sun C 2012 High-temperature piezoresistive pressure sensor based on implantation of oxygen into silicon wafer *Sens. Actuators A* **179** 277–82
- [104] Oysted K and Wisland D T 2005 Piezoresistive CMOS-MEMS pressure sensor with ring oscillator readout including/spl Delta-/spl Sigma/analog-to-digital converter on-chip *IEEE Custom Integrated Circuits Conf.* 511–4 (<https://ieeexplore.ieee.org/document/1568718>)
- [105] Dahlmann G, Hölzer G, Hering S and Schwarz U 2005 A modular CMOS foundry process for integrated piezoresistive pressure sensors *Advanced Microsystems for Automotive Applications* (Berlin: Springer) pp 413–24 (https://link.springer.com/chapter/10.1007%2F3-540-27463-4_30)
- [106] Chaehoi A, O'Connell D, Weiland D, Adamson R, Bruckshaw S, Ray S, Begbie M and Bruce J M 2010 Monolithic CMOS MEMS technology development: a

- piezoresistive-sensors case study *NSTI Nanotechnol. Conf. Expo* **2** 284–7 (<https://briefs.techconnect.org/papers/monolithic-cmos-mems-technology-development-a-piezoresistive-sensors-case-study/>)
- [107] Wang H-H, Hsu C-W, Liao W-H, Yang L-J and Dai C-L 2006 Micro pressure sensors of 50 μm size fabricated by a standard CMOS foundry and a novel post process *IEEE MEMS (Istanbul, Turkey)* pp 578–81 (<https://ieeexplore.ieee.org/document/1627865>)
- [108] Chang H-C, Liao S-C, Hsieh H-S, Wen J-H, Lai C-H and Fang W 2016 Magnetostrictive type inductive sensing pressure sensor *Sens. Actuators A* **238** 25–36
- [109] Shibata H, Ito M, Asakursa M and Watanabe K 1996 A digital hygrometer using a polyimide film relative humidity sensor *IEEE Trans. Instrum. Meas.* **45** 564–9
- [110] Fraden J 2016 *Handbook of Modern Sensors: Physics Designs, and Applications* (New York: LLC, Springer)
- [111] Manut A, Zoolfakar A S, Mamat M H, Ab Ghani N S and Zolkapli M 2020 Characterization of titanium dioxide (TiO_2) nanotubes for resistive-type humidity sensor *IEEE Int. Conf. on Semiconductor Electronics (Kuala Lumpur, Malaysia)* pp 104–7 (<https://ieeexplore.ieee.org/document/9166854>)
- [112] Hung C, Sung W, Chen S and Fang W 2019 Resistance-type humidity sensor using cnts sensing material with Al_2O_3 conformal coating for enhanced sensitivity *IEEE Transducers (Berlin, Germany)* pp 761–4 (<https://ieeexplore.ieee.org/document/8808689>)
- [113] Dai C-L, Liu M-C, Chen F-S, Wu C-C and Chang M-W 2006 A nanowire WO_3 humidity sensor integrated with micro-heater and inverting amplifier circuit on chip manufactured using CMOS-MEMS technique *Sens. Actuators B* **123** 896–901
- [114] Kang U and Wise K D 2009 A high-speed capacitive humidity sensor with on-chip thermal reset *IEEE Trans. Electron Devices* **47** 702–10
- [115] Kim J, Hong S, Lee J, Moon B and Kim K 2009 High sensitivity capacitive humidity sensor with a novel polyimide design fabricated by MEMS technology *IEEE Int. Conf. on Nano/Micro Engineered and Molecular Systems (Shenzhen, China)* pp 703–6 (<https://ieeexplore.ieee.org/document/5068676>)
- [116] Lazarus N and Fedder G K 2012 Designing a robust high-speed CMOS MEMS capacitive humidity sensor *J. Micromech. Microeng.* **22** 085021
- [117] Chen S, Chung V P J, Yao D and Fang W 2017 Vertically integrated CMOS-MEMS capacitive humidity sensor and a resistive temperature detector for environment application *IEEE Transducers (Kaohsiung, Taiwan)* pp 1453–4 (<https://ieeexplore.ieee.org/document/7994333>)
- [118] Chung V P J, Liang J K, Cheng C, Yip M and Fang W 2014 Development of a CMOS-MEMS RF-aerogel-based capacitive humidity sensor *IEEE Sensors (Valencia, Spain)* pp 190–3 (<https://ieeexplore.ieee.org/document/6984965>)
- [119] Chung V P J, Cheng C-L, Yip M-C and Fang W 2015 A CMOS capacitive vertical-parallel-plate-array humidity sensor with RF-aerogel fill-in for sensitivity and response time improvement *IEEE MEMS (Estoril, Portugal)* pp 767–70 (<https://ieeexplore.ieee.org/document/7051071>)
- [120] Dai C L 2006 A capacitive humidity sensor integrated with micro heater and ring oscillator circuit fabricated by CMOS-MEMS technique *Sens. Actuators B* **122** 375–80 (<https://www.sciencedirect.com/science/article/pii/S0925400506004369?via%3Dihub>)
- [121] Lazarus N, Bedair S, Lo C and Fedder G 2009 CMOS-MEMS capacitive humidity sensor *IEEE MEMS (Sorrento, Italy)* pp 268–71 (<https://ieeexplore.ieee.org/document/4805370>)
- [122] Chang C, Hong P, Yeh S, Lin Y, Lai M and Fang W 2020 Environmental sensing hub on single chip using double-side post-CMOS processes *IEEE MEMS (Vancouver, Canada)* pp 877–80 (<https://ieeexplore.ieee.org/document/9056143>)
- [123] Boltshauser T, Azeredo Leme C and Baltes H 1993 High sensitivity CMOS humidity sensors with on-chip absolute capacitance measurement system *Sens. Actuators B* **15** 75–80
- [124] Dai C L and Lu D H 2010 Fabrication of a micro humidity sensor with polypyrrole using the CMOS process *IEEE 5th Int. Conf. on Nano/Micro Engineered and Molecular Systems* pp 110–3 (<https://ieeexplore.ieee.org/document/5592158>)
- [125] Waber T, Sax M, Pahl W, Stufler S, Leidl A, Günther M and Feiertag G 2014 Fabrication and characterization of a piezoresistive humidity sensor with a stress-free package *J. Sens. Sens. Syst.* **3** 167–75
- [126] Boltshauser T, Schonholzer M, Brand O and Baltes H 1992 Resonant humidity sensors using industrial CMOS-technology combined with postprocessing *J. Micromech. Microeng.* **2** 205
- [127] Strembeck D, Robinson A M, Vermeulen F E, Seto M and Brown K B 1999 Humidity measurement using resonating CMOS microcantilever structures *IEEE Conf. on Electrical and Computer Engineering* pp 1658–61
- [128] Seo J and Han H 2001 Water diffusion studies in polyimide thin films *J. Appl. Polym. Sci.* **82** 731–7
- [129] Cheng C-L, Tsai M-H and Fang W 2015 Determining the thermal expansion coefficient of thin films for a CMOS MEMS process using test cantilevers *J. Micromech. Microeng.* **25** 025014
- [130] Fang W, Li S S, Chiu Y and Li M-H 2021 *3D and Circuit Integration of MEMS* (Hoboken, NJ: Wiley-VCH)
- [131] Simon I, Barsan N, Bauer M and Weimar U 2001 Micromachined metal oxide gas sensors: opportunities to improve sensor performance *Sens. Actuators B* **73** 1–26
- [132] Liu S F, Moh L C H and Swager T M 2015 Single-walled carbon nanotube–metalloporphyrin chemiresistive gas sensor arrays for volatile organic compounds *Chem. Mater.* **27** 3560–3
- [133] Bakker E and Telting-Diaz M 2002 Electrochemical sensors *Anal. Chem.* **74** 2718–800
- [134] Wana H, Yin H, Lin L, Zeng X and Mason A J 2018 Miniaturized planar room temperature ionic liquid electrochemical gas sensor for rapid multiple gas pollutants monitoring *Sens. Actuators B* **255** 638–46
- [135] Sharma B and Kim J-S 2018 MEMS based highly sensitive dual FET gas sensor using graphene decorated Pd-Ag alloy nanoparticles for H_2 detection *Sci. Rep.* **8** 5902
- [136] Ingemar L, Hans S, Fredrik W, Mats E, Christina K-R and Anita L-S 2007 Twenty-five years of field effect gas sensor research in link öping *Sens. Actuators B* **121** 247–62
- [137] Dinha T-V, Choi I-Y, Son Y-S and Kim J-C 2016 A review on non-dispersive infrared gas sensors: improvement of sensor detection limit and interference correction *Sens. Actuators B* **231** 529–38
- [138] Wolfbeis O S 2005 Materials for fluorescence-based optical chemical sensors *J. Mater. Chem.* **15** 2657–69
- [139] Bartlett P N and Guerin S 2003 A Micromachined Calorimetric Gas Sensor: an Application of Electrodeposited Nanostructured Palladium for the Detection of Combustible Gases *Anal. Chem.* **75** 126–32
- [140] Bindra P and Hazra A 2018 Capacitive gas and vapor sensors using nanomaterials *J. Mater. Sci., Mater. Electron.* **29** 6129–48 (<https://link.springer.com/article/10.1007%2Fs10854-018-8606-2>)
- [141] Baselt D R, Fruhrberger B, Klaassen E, Cemalovic S, Britton C L Jr., Patel S V, Mlsna T E, McCorkle D and

- Warmack B 2003 Design and performance of a microcantilever-based hydrogen sensor *Sens. Actuators B* **88** 120–31
- [142] Kacem N, Arcamone J, Perez-Murano F and Hentz S 2010 Dynamic range enhancement of nonlinear nanomechanical resonant cantilevers for highly sensitive NEMS gas/mass sensor applications *J. Micromech. Microeng.* **20** 045023
- [143] Penz M, Avers P, Cassano G, Wlodarski W and Kalantar-Zadeh K 2007 Layered SAW gas sensor with single-walled carbon nanotube-based nanocomposite coating *Sens. Actuators B* **127** 168–78
- [144] Tzeng T et al 2016 A portable micro gas chromatography system for lung cancer associated volatile organic compound detection *IEEE J. Solid State Circuits* **51** 259–72
- [145] Mayes A G, Blyth J, Kyroläinen-Reay M, Millington R B and Lowe C R 1999 A holographic alcohol sensor *Anal. Chem.* **71** 3390–6
- [146] Robert Bosch Gas sensors (available at: www.bosch-sensortec.com/products/environmental-sensors/gas-sensors-bme680/)
- [147] Figaro Gas Sensors & Modules (available at: www.figarosensor.com/product/sensor/)
- [148] Yin H, Mu X, Li H, Liu X and Mason A J 2018 CMOS monolithic electrochemical gas sensor microsystem using room temperature ionic liquid *IEEE Sens. J.* **18** 7899–906
- [149] Sensirion Multi-Pixel Gas Sensors (available at: www.sensirion.com/en/environmental-sensors/gas-sensors/)
- [150] Choopun S, Hongsih N and Wongrat E 2012 Metal-oxide nanowires for gas sensors *Nanowires—Recent Advances* (London, UK: IntechOpen Limited) pp 3–24
- [151] Comini E, Faglia G and Sberveglieri G 2009 *Solid State Gas Sensing* (New York: LLC, Springer)
- [152] Shimizu Y and Egashira M 1999 Basic aspects and challenges of semiconductor gas sensors *MRS Bull.* **24** 18–24
- [153] Ruhland B, Becker T and Müller G 1998 Gas-kinetic interactions of nitrous oxides with SnO₂ surfaces *Sens. Actuators B* **50** 85–94
- [154] Andrew P L and Brian J R 1999 Temperature modulation in semiconductor gas sensing *Sens. Actuators B* **60** 35–42
- [155] Jing Z and Zhan J 2008 Fabrication and gas-sensing properties of porous ZnO nanoplates *Adv. Mater.* **20** 4547–51
- [156] Suehle J S, Cavicchi R E, Gaitan M and Semancik S 1993 Tin oxide gas sensor fabricated using CMOS micro-hotplates and *in-situ* processing *IEEE Electron Device Lett.* **14** 118–20
- [157] Mutinati G C et al 2014 Optimization of CMOS integrated nanocrystalline SnO₂ gas sensor devices with bimetallic nanoparticles *Procedia Eng.* **87** 787–90
- [158] Lackner E, Krainer J, Wimmer-Teubenbacher R, Sosada F, Gspan C, Rohrachner K, Wachmann E and Koeck A 2016 CMOS integrated nanocrystalline SnO₂ gas sensors for CO detection *Procedia Eng.* **168** 297–300
- [159] Lee Y-C, Cheng S-W, Lin Y-C and Fang W 2019 Monolithic integrated CMOS-MEMS MOS type gas sensor and novel heater for sensitivity and power consumption enhancement *IEEE Transducers & Eurosensors (Berlin, Germany)* pp 1389–92 (<https://ieeexplore.ieee.org/document/8808361>)
- [160] Lee Y-C, Yang P-L, Cheng C-I and Fang W 2018 Design and fabrication of MOS type gas sensor with vertically integrated heater using cmos-mems technology *Proceedings* **2** 772
- [161] Ali S Z, Udrea F, Milne W I and Gardner J W 2008 Tungsten-based SOI microhotplates for smart gas sensors *J. Microelectromech. Syst.* **17** 1408–17
- [162] Guha P K, Ali S Z, Lee C C C, Udrea F, Milne W I, Iwaki T, Covington J A and Gardner J W 2007 Novel design and characterisation of SOI CMOS micro-hotplates for high temperature gas sensors *Sens. Actuators B* **127** 260–6
- [163] Choi K J and Jang H W 2010 One-Dimensional Oxide nanostructures as gas-sensing materials: review and issues *Sensors* **10** 4083–99
- [164] Wang S, Yang J, Zhang H, Wang Y, Gao X, Wang L and Zhu Z 2015 One-pot synthesis of 3D hierarchical SnO₂ nanostructures and their application for gas sensor *Sens. Actuators B* **207** 83–9
- [165] Bhati V S, Hojamberdiev M and Kumar M 2020 Enhanced sensing performance of ZnO nanostructures-based gas sensors: a review *Energy Rep.* **6** 46–62
- [166] Lu C and Chen Z 2009 High-temperature resistive hydrogen sensor based on thin nanoporous rutile TiO₂ film on anodic aluminum oxide *Sens. Actuators B* **140** 109–15
- [167] Shendage S S, Patil V L, Vanalakar S A, Patil S P, Harale N S, Bhosale J L, Kim J H and Patil P S 2017 Sensitive and selective NO₂ gas sensor based on WO₃ nanoplates *Sens. Actuators B* **240** 426–33
- [168] Liu X, Jiang L, Jiang X, Tian X, Sun X, Wang Y, He W, Hou P, Deng X and Xu X 2018 Synthesis of Ce-doped In₂O₃ nanostructure for gas sensor applications *Appl. Surf. Sci.* **428** 478–84
- [169] Lado F and Selberherr S 2015 Performance and stress analysis of metal oxide films for CMOS-integrated gas sensors *Sensors* **15** 7206–27
- [170] Mutinati G C, Brunet E, Steinhauer S, Köck A, Teva J, Kraft J, Siegert J, Schrank F and Bertagnolli E 2012 CMOS-integrable ultrathin SnO₂ layer for smart gas sensor devices *Procedia Eng.* **47** 490–3
- [171] Yu Q, Boussaid F, Bermak A and Tsui C-Y 2018 Room-temperature dual-mode CMOS gas-FET sensor for diabetes detection *IEEE Int. Symp. on Circuits and Systems (Florence, Italy)* pp 1–4 (<https://ieeexplore.ieee.org/document/8351086>)
- [172] Yu Q, Zhong X, Boussaid F, Bermak A and Tsui C Y 2018 High performance high density gas-FET array in standard CMOS *IEEE Symp. on VLSI Technology (Honolulu, HI, USA)* pp 39–40 (<https://ieeexplore.ieee.org/document/8510700>)
- [173] Chowdhury M F, Hopper R, Ali S Z, Gardner J W and Udrea F 2016 MEMS infrared emitter and detector for capnography applications *Procedia Eng.* **168** 1204–7
- [174] Lee Y-C, Cheng S-W, Cheng C-L and Fang W 2017 Design and implementation of gas sensor array based on fluorescence quenching detection using CMOS-MEMS process *IEEE Transducers (Kaohsiung, Taiwan)* pp 672–5 (<https://ieeexplore.ieee.org/document/7994138>)
- [175] Lee Y-C, Cheng S-W and Fang W 2019 Monolithic integrated CMOS-MEMS fluorescence quenching gas sensor and resistive temperature detector (RTD) for temperature compensation *IEEE Transducers & Eurosensors (Berlin, Germany)* pp 1293–6 (<https://ieeexplore.ieee.org/document/8808639>)
- [176] Hopper R, Ali S, Chowdhury M, Boual S, De Luca A, Gardner J W and Udrea F 2014 A CMOS-MEMS thermopile with an integrated temperature sensing diode for Mid-IR thermometry applications *Eurosensors* **87** 1127–30 (<https://www.sciencedirect.com/science/article/pii/S1877705814024783?via%3Dihub>)
- [177] STMicroelectronics 9-axis iNEMO inertial module (IMU): 3D magnetometer, 3D accelerometer, 3D gyroscope with I2C and SPI (available at: www.st.com/en/mems-and-sensors/lsm9ds1.html#)

- [178] Sun C-M, Tsai M-H, Wang C, Liu Y-C and Fang W 2009 Implementation of a monolithic TPMS using CMOS-MEMS technique *IEEE Transducers (Denver, CO, USA)* pp 1730–3 (<https://ieeexplore.ieee.org/document/5285736>)
- [179] Kim K-D et al 2018 A 100mK-NETD 100ms-startup-time 80×60 micro-bolometer CMOS thermal imager integrated with a 0.234mm² 1.89μVrms noise 12b biasing DAC 2018 *IEEE Int. Solid—State Circuits Conf.—(ISSCC) (San Francisco, CA, USA)* pp 192–4 (<https://ieeexplore.ieee.org/document/8310249>)
- [180] Shi X, Liu D, Chen Z, Chen G, Huang S, Lu W and Zhang Y 2019 A low-power single-slope based 14-bit column-level ADC for 384×288 uncooled infrared imager *IEEE ASICON 2019 (Chongqing, China)* p 8983526 (<https://ieeexplore.ieee.org/document/8983526>)
- [181] Sensirion Digital Humidity Sensor SHT3x (RH/T) (available at: www.sensirion.com/en/environmental-sensors/humidity-sensors/digital-humidity-sensors-for-various-applications/)
- [182] Texas Instrument HDC1080 Low Power, High Accuracy Digital Humidity Sensor with Temperature Sensor (available at: www.ti.com/document-viewer/HDC1080/datasheet)
- [183] Rotronic Humidity (available at: www.rotronic.com/en-us/humidity-measurement-feuchtemessung-temperaturmessung/humidity-measurement-feuchte-messung.html)
- [184] Vaisala Products (available at: www.vaisala.com/en/products/instruments-sensors-and-other-measurement-devices/instruments-industrial-measurements/hmt330)
- [185] Taiwan Semiconductor Manufacturing MEMS Technology (available at: www.tsmc.com/english/dedicatedFoundry/technology/specialty/mems)
- [186] TDK-invensense Technology (available at: <https://invensense.tdk.com/technology/>)
- [187] ITRS From Moore's Law to NTRS to ITRS to IRDS™ (available at: <https://irds.ieee.org/component/content/article/8-home/4-what-is-the-irds>)
- [188] Sensirion (available at: www.sensirion.com/en/environmental-sensors/carbon-dioxide-sensors/carbon-dioxide-sensors-co2/)